JOURNAL OF GEOPHYSICAL RESEARCH, VOL. 105, NO. C2, PAGES 3379–3400, FEBRUARY 15, 2000

High-frequency ice motion and divergence in the Weddell Sea

Laurie Padman

Earth and Space Research, Seattle, Washington

Christoph Kottmeier[1]

Alfred Wegener Institute for Polar and Marine Research, Bremerhaven, Germany

Abstract. We describe the spatial variability of high frequency ice velocity in the Weddell Sea using satellite-tracked ice-mounted buoys. Ice motion is analyzed separately for "diurnal" (1/36-1/18 cph) and "semidiurnal" (1/18-1/6 cph) bands. Ice motion in both bands is caused by a combination of ocean tidal currents and wind stress. Monthly mean diurnal band ice speeds over the deep basin range from 2 to 4 cm s^{-1} depending on wind stress variance and ice concentration (C_{ice}). Higher speeds (~10 cm s^{-1}) are found in the semidiurnal band in regions of low C_{ice}, notably the northern Weddell Sea, where the ice velocity is dominated by the inertial response to wind stress variations. Monthly mean tidal band ice speeds over the continental slope and shelves often exceed 10 cm s^{-1}. We use comparisons between buoy velocities, moored current meter data, and an ocean tidal model to demonstrate that ice motion is frequently a good indicator of ocean tidal currents in strongly tidal regions. The standard deviation of the divergence of ocean tidal currents estimated from an ocean-only tidal model is small ($<0.1\times10^{-6}$ s^{-1}) over most of the Weddell Sea but has values of $1\text{-}5\times10^{-6}$ s^{-1} along the Ronne Ice Front and the continental shelf break. High frequency ice divergence is dominated by ice response to wind stress rather than by tides except along the shelf break and ice fronts. In these tidally dominated regions the periodic divergence maintains a mean lead (open water) area of ~2-5%. This increased lead fraction implies an increase in area-averaged winter ocean-to-atmosphere heat exchange rate of ~4-10 W m^{-2} and an increase in salt flux into the upper ocean as new ice forms in the leads.

1. Introduction

The role of ocean tides in forcing sea ice drift and periodic divergence has been recognized for at least a century [see, e.g., *Nansen*, 1898, p. 180]. For climate studies the importance of ice divergence is that the winter flux of heat from the ocean to the polar atmosphere can be 1-2 orders of magnitudes higher through the open water of leads than through the adjacent sea ice [*Maykut*, 1986; *Launiainen and Vihma*, 1994]. A small mean fraction of leads in pack ice can therefore greatly increase the area- and time-averaged ocean-to-atmosphere heat loss, ice formation rate, and salt flux into the upper ocean. The new ice in the leads is crushed into ridges at floe edges during the convergent phase, permitting additional rapid ice growth during the divergent phase. This "ice accordian" process is particularly efficient for high-frequency divergence-convergence cycles. More rapid cycling results in a thinner mean new ice thickness and thus more mean heat loss and brine rejection during new ice growth. An understanding of high-frequency ice motion is also of value when attempting to estimate mean ice motion by tracking features between pairs of satellite images that may be separated in time by one to several days [*Drinkwater*, 1998], so that the tidal motion is aliased into the mean drift estimates.

The Weddell Sea (Figure 1) is the major source for Antarctic Bottom Water (AABW) that is found throughout the World Ocean [*Broecker et al.*, 1998]. Air-sea interactions around the Weddell Sea perimeter are responsible for creating the cold and dense shelf waters that are necessary for the production of AABW and the colder and denser Weddell Sea Bottom Water [see *Gordon*, 1998]. *De Veaux et al.* [1993] demonstrated empirically that the distribution of ice concentration was related to topography, being dependent on both water depth and bottom slope. We know that tides are a major source of oceanic kinetic energy over shallow water and steep topography [*Robertson et al.*, 1998], so we ask: Are tides at least partly responsible for the observed distributions of sea ice motion and concentration? Given this research focus, the geographical features of most significance are those that influence the distribution of tidal energy and divergence. These features include the shelf break and the ice fronts of the Ronne, Filchner, and Larsen Ice Shelves, which are the floating extensions of thick glacial ice flowing off Antarctica. The typical water depth over the continental shelf is ~400-500 m, thus the shelf break in Figure 1 is approximately defined by the 500 m isobath. Water depths in the center of the Weddell Sea exceed 4000 m. Depth data are, however, sparse over much of the western and southwestern Weddell Sea, and this lack of data severely limits our ability to accurately model ocean tidal currents [*Padman et al.*, 1998].

With our interest in tides we focus on high-frequency ice motion, defined here as variability between 1/36 and 1/6 cph.

[1]Now at Institut für Meteorologie und Klimaforschung, Universität Forschungszentrum Karlsruhe, Karlsruhe, Germany.

Copyright 2000 by the American Geophysical Union.

Paper number 1999JC900267.
0148-0227/00/1999JC900267$09.00

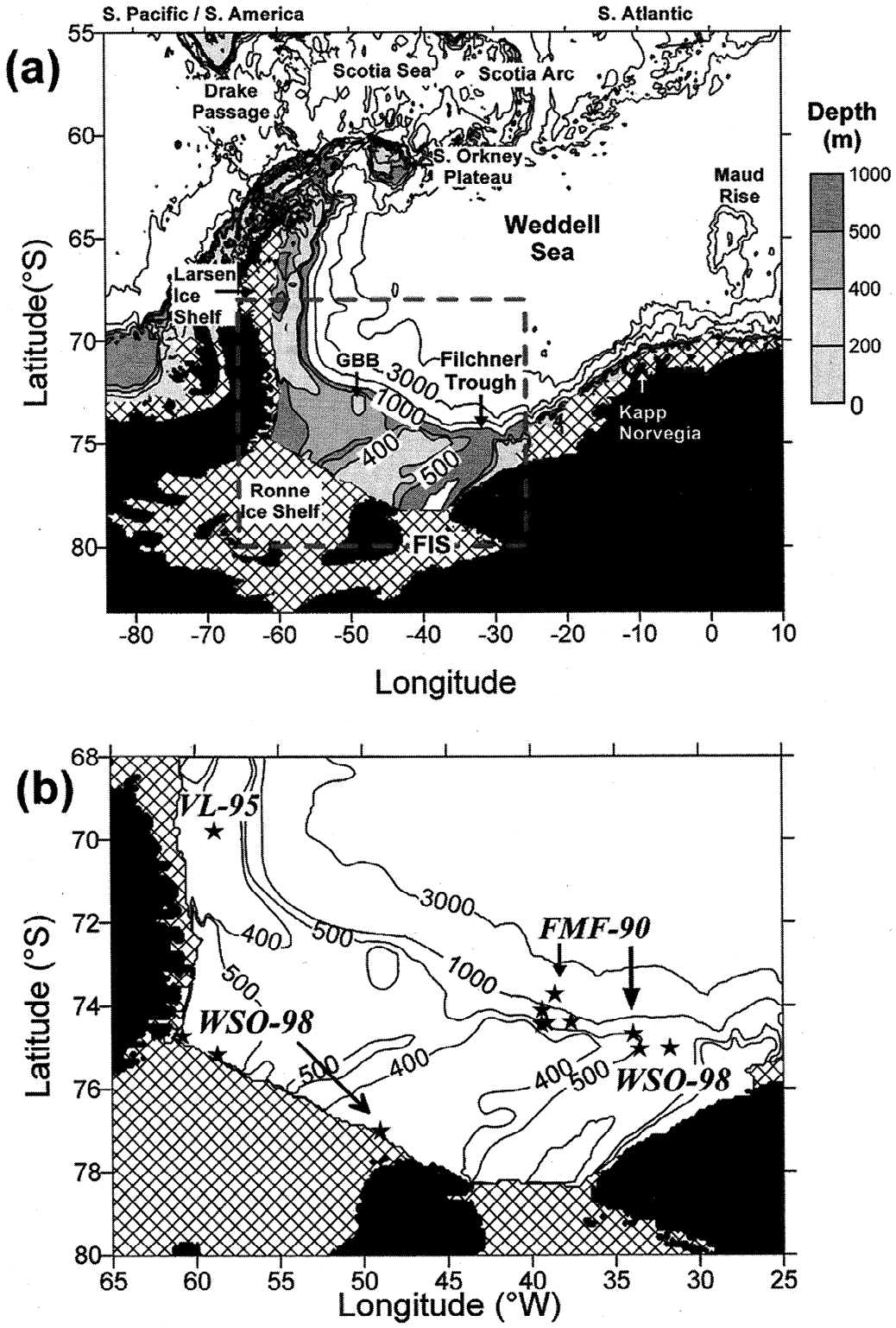

Figure 1. (a) Principal topographic features in the Weddell Sea region. The General Belgrano Bank (GBB: ~73°S, 48°W) and the Filchner Ice Shelf (FIS) are indicated. (b) Locations, indicated by stars, of current measurements on the southern Weddell Sea shelf and slope, reported by *Foldvik et al.* [1990] (*FMF-90*) and *Woodgate et al.* [1998] (*WSO-98*). The location of the tidal ice motion measurements by *Viehoff and Li* [1995] near 70°S, 59°W is also indicated (*VL-95*). Depths are in meters.

Various authors [e.g., *Rowe et al.*, 1989; *Viehoff and Li*, 1995; *Kottmeier and Sellmann*, 1996; *Kottmeier et al.*, 1992, 1997; *Geiger et al.*, 1998a] have noted the influence of ocean tides on ice motion. However, ice motion in this frequency band can also be caused by its direct response to high-frequency wind stress variability and a near-resonant response to wind stress pulses. The first process encompasses ice motion in phase with fluctuations of high-frequency wind stress. Most wind variability occurs with periods of several days; however, ~20% of the wind velocity variance occurs at frequencies

>1/36 cph [*Kottmeier et al.*, 1997]. The second process entails the setup of ice velocity oscillations with frequencies near the local inertial frequency f, which ranges from ~1/14 to 1/12 cph over the latitude range 60-85°S. We will show that both tidal and wind forcing contribute significantly to ice motion when averaged over the Weddell Sea but that the spatial patterns for these processes are very different.

Time series of the paths of clusters of satellite-tracked buoys show that spatial velocity gradients (shear, strain, curl, and divergence) can also contain significant high-frequency energy [*Kottmeier et al.*, 1997; *Geiger et al.*, 1998a, b]. As was noted above, periodic divergence of the ice pack can increase the mean heat loss from the ocean to the atmosphere. Shear and strain help to break up the ice cover into smaller floes and make the sea ice more responsive to local external stresses. *Kowalik and Proshutinsky* [1994], who coupled a high-resolution barotropic ocean tide model to a dynamic ice model, concluded that ice response to tides must be included in realistic models of the thermohaline forcing of the Arctic Ocean. We propose that this is also true for the Weddell Sea. This is not a novel hypothesis [see, e.g., *Foldvik and Gammelsrød*, 1988; *Kottmeier and Sellmann*, 1996]. However, we extend these studies by a more detailed analysis of available buoy data and comparisons with ocean data and an ocean-only tidal model.

In this paper we first describe the analysis procedures for obtaining high-frequency ice motion and gradient quantities from time series of the positions of clusters of satellite-tracked buoys (section 2). The spatial distributions of ice speed in two broadly defined "tidal" bands, diurnal (1/36-1/18 cph) and semidiurnal (1/18-1/6 cph), are then presented (section 3). The term "tidal band" refers to the entire frequency range of 1/36-1/6 cph, even though much of the ice motion at these frequencies is associated with wind forcing rather than ocean tides. We then describe a depth-averaged ocean-only tide model that we use to interpret the drifter observations (section 4). We conclude with a discussion (section 5) including an assessment of the validity of the free drift approximation and the oceanographic relevance of the modeled and measured tidal band ice divergence.

The influence of lead fraction on average air-sea heat fluxes, ice formation, and salt flux to the upper ocean in the western Weddell Sea will be quantified in a future study (O. Eisen, personal communication, 1999) on the basis of a kinematic-thermodynamic sea ice model and the time series of ice divergence from one buoy cluster.

2. Methodology for Obtaining Tidal Band Ice Motion From Buoys

2.1. Buoy Data Sets and Tidal Band Ice Velocity Determination

Autonomous buoys deployed on the Weddell Sea pack ice have provided large-scale wind, temperature, and ice motion statistics from this region [*Kottmeier et al.*, 1997]. The buoys that we consider here were deployed during the Winter Weddell Sea Project 1986 (WWSP86) [*Augstein*, 1986], during the *Polarstern* cruises ANT-X [*Spindler et al.*, 1993] in 1992 and ANT-XII [*Jokat and Oerter*, 1997] in 1995, and

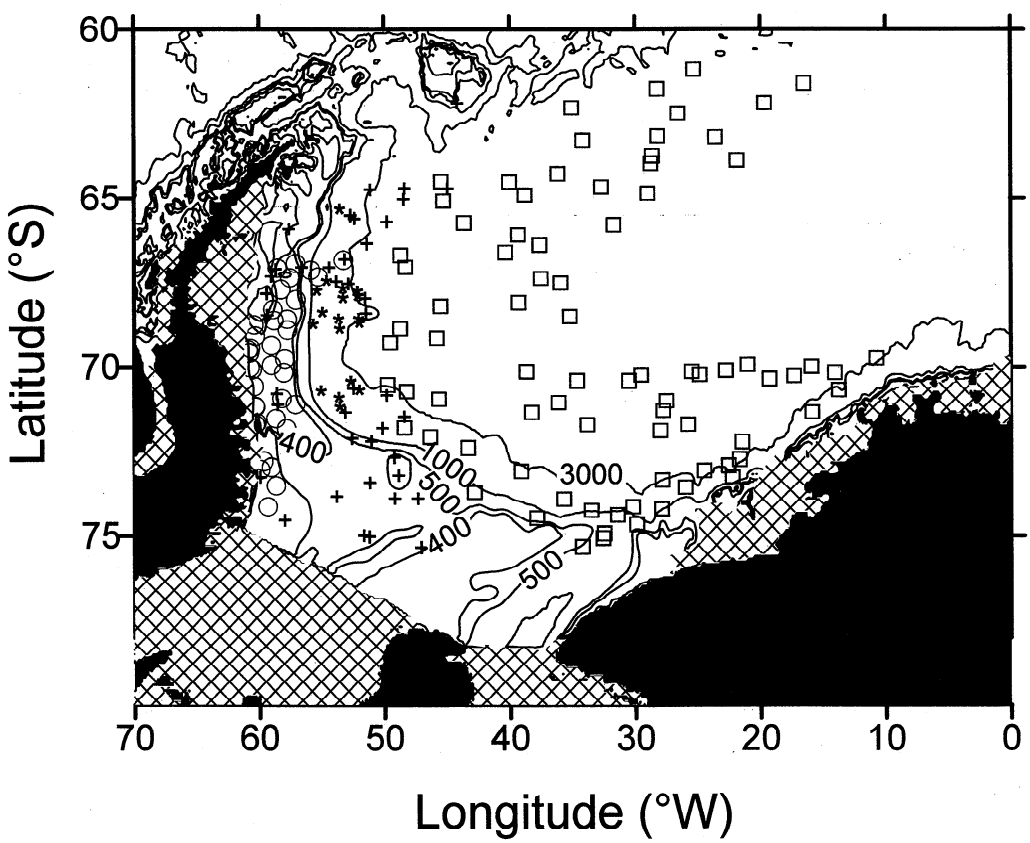

Figure 2. Monthly location of every buoy used in the ice motion analysis. Drifters released in 1986, 1992, and 1995 are indicated by open squares, open circles, and pluses, respectively. Deployments during Ice Station Weddell are indicated by asterisks. Depths are in meters.

in the western Weddell Sea around Ice Station Weddell 1 (ISW-1) in 1992 [*Gordon and Ice Station Weddell Group of Principal Investigators and Chief Scientists*, 1993; *Muench and Gordon,* 1995; *Geiger et al.*, 1998a, b]. Buoy locations were determined from Doppler shifts of the transmitted signals observed at different satellite positions. The accuracy of individual buoy positions from the Argos satellite positioning system is ~350 m. Accuracies of 150 m can now be achieved by improved processing methods by Argos CLS but were not available for the full data set on a regular basis. The Argos system obtained ~20 position estimates per day for each buoy. Ice drift velocity, $\mathbf{D}(t)=(d_x, d_y)$, for each buoy was obtained from the time series of buoy location. A regularly spaced time series with a resolution of 3 hours was generated using cubic spline interpolation. Long gaps were filled by linear interpolation. The geographical distribution of these data is shown in Figure 2. The mean ice drift paths were clockwise with the mean flow of the Weddell Gyre [*Orsi et al.,* 1993; *Fahrbach et al.,* 1994, 1998].

The momentum balance for drifting sea ice involves wind and water stresses, the pressure gradient associated with any geostrophic current, Coriolis forces, internal stresses, and advective and local accelerations. Even without the latter two terms, the forces acting on the ice generally cause a nonlinear response of ice motion to winds and currents. Despite these difficulties, ice motion can be a useful marker of tidal currents, as is demonstrated below.

The linear model [*Thorndike and Colony*, 1982] approximates the time-dependent ice motion by

$$\mathbf{D}(t)=\mathbf{A}\mathbf{V}_g(t)+\mathbf{C}_g+\varepsilon(t), \qquad (1)$$

where, $\mathbf{V}_g(t)$ is the geostrophic wind, $\mathbf{A}$ is a constant complex multiplier linearly relating ice drift fluctuations to geostrophic wind variations, $\mathbf{C}_g$ is the constant mean (not wind-correlated) component of the ice motion, and $\varepsilon(t)$ is the residual drift. The vector $\mathbf{C}_g$ sums all mean effects that are not represented by the geostrophic wind, specifically the mean effects of internal ice stress and ocean surface tilt. The residual $\varepsilon(t)$ accounts for ice drift that is neither wind-related nor caused by the constant ocean current. It not only includes ocean tidal motion and higher-frequency fluctuations of internal stress but also "noise" from wind velocity and ice drift observational errors.

Equation (1), without ε, is used as a regression equation to calculate the optimum constants $\mathbf{A}$ and $\mathbf{C}_g$ for 30 day periods (240 three-hourly estimates of $\mathbf{D}(t)$ and $\mathbf{V}_g(t)$). It is found that for periods >0.5 days the linear model generally accounts for >60% of the total variance of drift speeds except for the region west of 45°W and south of ~68°S in the southwestern Weddell Sea. In the latter region, relative explained variances vary from 15 to 70%, and the modulus of the complex multiplier $|\mathbf{A}|$ ranges from 0.2×10^{-2} to 0.9×10^{-2}, whereas it is above 1×10^{-2} in all other regions. The weaker and nonlinear correspondence of ice motion to the winds in this region has previously been attributed to more frequent events associated with tidal influences [*Kottmeier and Sellmann*, 1996] and also to large internal stresses.

Variances explained by the linear model (1) were recalculated for ice drift and geostrophic wind data in the Weddell Sea after low-pass filtering at 36 hours to eliminate direct tidal effects. Relative explained variances for the southwestern Weddell Sea became significantly larger, between 50 and 90%, and did not systematically differ from those for other regions. However, $|\mathbf{A}|$ remained below 1×10^{-2}. The linear response of ice drift to winds in the period band of synoptic processes (36 hours and longer) is therefore a critical element of ice motion in all parts of the Weddell Sea, even though the ratio of drift speed to geostrophic wind speed ($|\mathbf{A}|$) varies between regions. Following (1), this implies that mean, non-wind-forced ocean currents are simply additive to the mean wind-related drift.

At semidiurnal and diurnal periods, ice motion and winds are almost uncorrelated in the western Weddell Sea, and the wind variance in these bands rarely exceeds 20% of the total wind variance [*Kottmeier et al.*, 1997]. The time series of the residual ε was compared to the original 36 hour high-pass filtered ice drift and was found to be very similar. This exercise shows that ice drift observations at semidiurnal and diurnal periods in the southwestern Weddell Sea provide useful information on tidal effects in the upper ocean. The amplitudes of ice drift fluctuations therefore are at least qualitative estimates of ocean tidal motion.

The ice response to ocean currents in the tidal band is expected to be affected by internal ice stresses. We know, from simultaneous measurements of upper ocean currents and ice motion in the Arctic, that tidal band ice velocity can be very different from ocean tidal currents [*Padman et al.*, 1992]. Near the Yermak Plateau in the eastern Arctic in early spring, diurnal band ice speeds of only 3 cm s^{-1} were measured where the diurnal ocean tidal current was 25 cm s^{-1}. This lack of ice response was attributed to the small spatial scales of ocean tidal current variability (which are comparable to the topographic slope scales [see *Robertson et al.,* 1998, Figure 5], relative to the distance over which the ice pack effectively acts as a single rigid sheet and thus integrates the tide-applied ocean-ice stress. This latter scale is large near the Yermak Plateau in winter because of the high ice concentration and mean thickness, and the mean convergence associated with the Transpolar Drift as the ice leaves the Arctic Basin through Fram Strait. Other published measurements reported by *Padman et al.* [1992] demonstrated that tidal band ice velocities could be much greater in the same region in summer, when the ice was weaker and thus less able to resist internal stresses. Similar seasonal variation can be expected for the Weddell Sea pack ice, which undergoes a pronounced seasonal cycle. *Rowe et al.* [1989] suggested that internal ice stresses were responsible for the observed reduction in tidal frequency ice motion during the austral winter, for the one drifter that they analyzed. However, as we will show below, much of the variability seen in individual drift tracks is truly spatial rather than temporal, and so, Rowe's conclusion must be regarded with caution.

Ice distribution in the Antarctic has been monitored with satellites for over 2 decades. The Special Sensor Microwave Imager (SSM/I) has provided ice concentration C_{ice} estimates approximately once per day since 1987. High C_{ice} values are found in the western portion of the Weddell Sea, which is a region of frequent onshore wind stress and mean ice convergence [*Kottmeier and Sellmann*, 1996]. This is illustrated in Figure 3 where we show the fraction of time that C_{ice} in each SSM/I satellite pixel location exceeds 90% (denoted C_{90}) during the period 1988-1995. In Figure 3, contour intervals are closely spaced for C_{90}>80%. Figure 3 is intended as a qualitative guide to regions where free drift may usually be valid (low values of C_{90}) and to suggest that in regions of persistently high C_{ice} the small perturbations in C_{90} are related to topography and perhaps therefore also to tides.

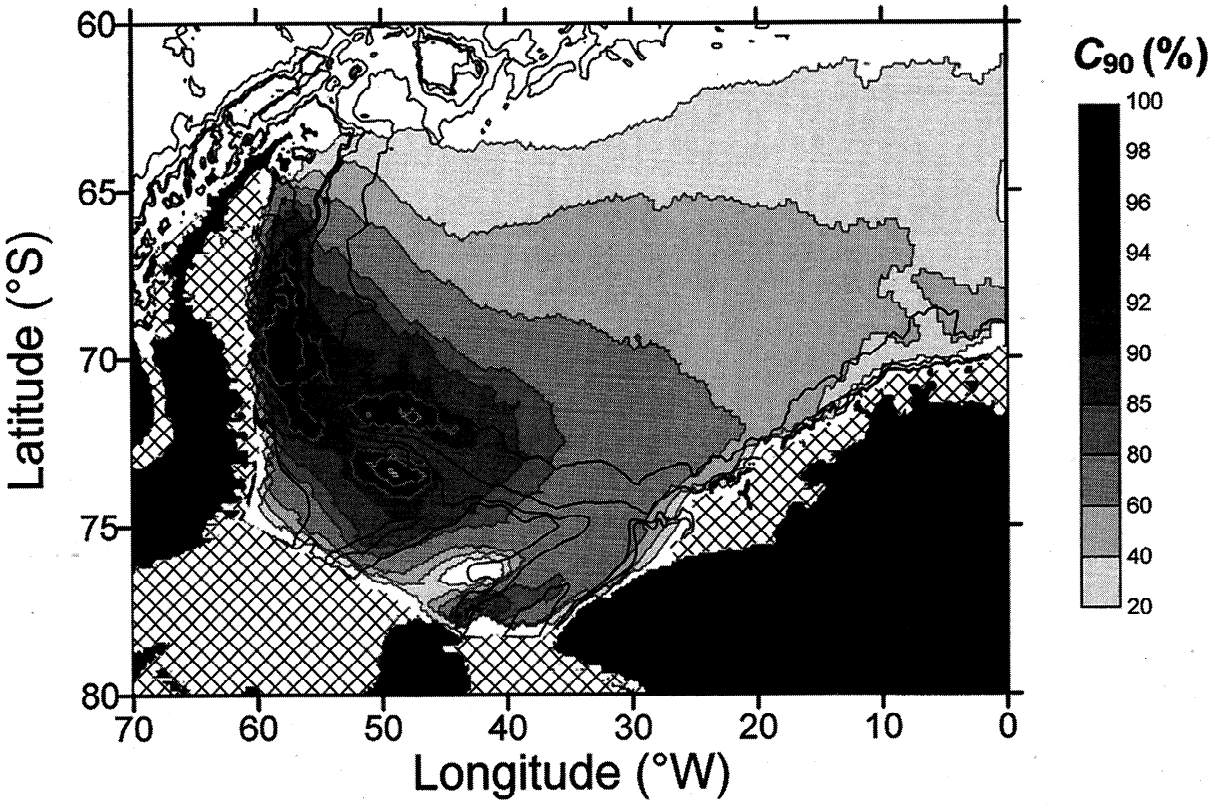

Figure 3. Percentage of time that the Special Sensor Microwave Imager satellite reported ice concentration above 90% (denoted C_{90} in the text), for the period 1988-1995. Data were provided by the National Snow and Ice Data Center. The 400, 500, 1000, and 3000 m isobaths are shown as solid lines (see Figure 1). The ranges of shading are not evenly spaced: intervals are much narrower for high values of C_{90}.

In the southern Weddell Sea, there is a trough of slightly lower C_{90} along the shelf break (roughly, the 500 m isobath) from near 40° to ~55°W. We shall return to Figure 3 in section 5.2.

2.2. Tidal Analysis of Ice Motion

The usual method for tidal analysis of ocean currents involves a multivariate least squares fit of sine and cosine waves at the known tidal frequencies [see, e.g., *Foreman*, 1978]. The total analyzed record length determines the number of constituents that can be numerically resolved (although additional constituents can be obtained by inferring the spectrally inseparable constituents from the resolved constituents). The four most energetic constituents are O_1 (period≈25.82 hours) and K_1 (23.93 hours) in the diurnal band, and M_2 (12.42 hours) and S_2 (12.00 hours) in the semidiurnal band. While the minimum required record length for resolving each of these pairs is ~15 days, in practice, much longer records are required to partition the total energy accurately between constituents. The method assumes that the amplitude and phase of constituents is stationary. For currents obtained at fixed moorings, some nonstationarity arises because of such processes as nonlinear interactions with seasonally varying "mean" flows and temporal variability in the baroclinic component of the total tidal current. Fortunately the kinetic energy of the baroclinic tide in the Weddell Sea is usually small relative to the more stable barotropic component.

For ice velocity, $\mathbf{D}(t)=(d_x(t), d_y(t))$, nonstationarity is also caused by the mean drift of the ice through a region of varying amplitude and/or phase. Even assuming free drift, the quality of a multiconstituent tidal analysis is reduced by any significant mean drift. For much of the present study we therefore use simplified measures of semidiurnal and diurnal currents. For each frequency band we first bandpass filter $d_x(t)$ and $d_y(t)$ for each buoy and then calculate time series of ice speed $|\mathbf{D}(t)|$. The mean ice speed is then obtained by averaging $|\mathbf{D}(t)|$ for 50%-overlapping 15 day intervals. These values are denoted D_d and D_{sd} for the diurnal and semidiurnal bands, respectively. For contouring purposes the values of D_d and D_{sd} were assigned to the buoy's geographic position at the center of each analysis time interval.

Remember that the tidal bands as defined previously are quite broad, and so, tidal band ice motion includes some contribution due to wind stress. Throughout our domain, wind-forced near-inertial oscillations are included in D_{sd}.

2.3. Differential Kinematic Parameters

Deployment of three or more buoys in a coherent array (which we call a "cluster") allows spatial derivatives of $\mathbf{D}(t)$ to be calculated. The method is as follows. Each cluster consists of K buoys for which we have velocity data ($\mathbf{D}_i(x,y,t)$: i=1…K) at N regular time steps. We fit linear functions to d_x and d_y at each time step according to a least squares minimization, over the K buoys, of

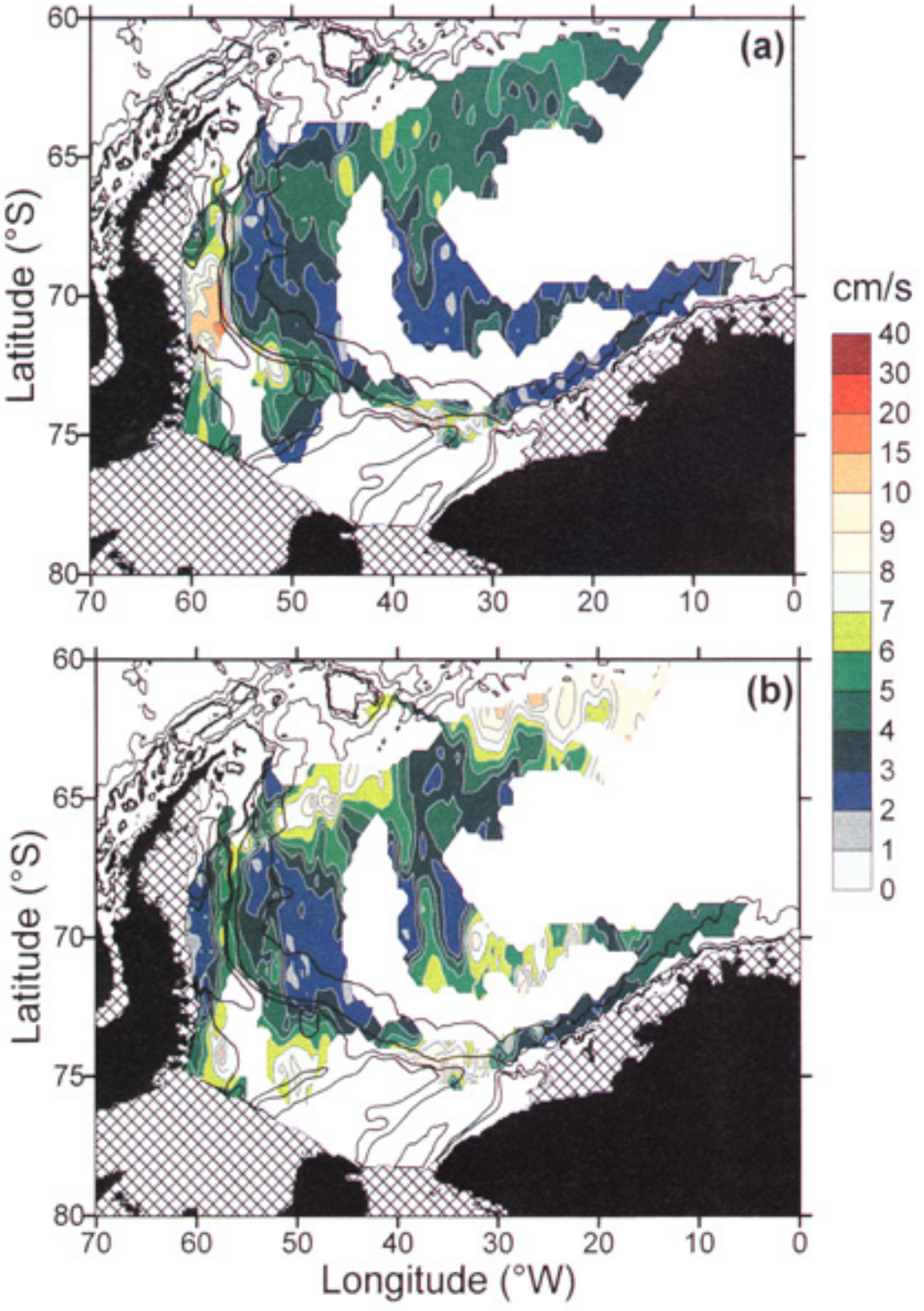

Plate 1. (a) Mean measured diurnal band ice speed D_d from drifting buoys. The 400, 500, 1000, and 3000 m isobaths are shown as solid lines (see Figure 1). (b) Mean measured semidiurnal band ice speed D_{sd} from drifting buoys. The color ranges are not evenly spaced. The averaging interval for speeds is 15 days.

$$d_x(x,y,t)=b_1(t)x+b_2(t)y+b_3(t)$$
$$d_y(x,y,t)=c_1(t)x+c_2(t)y+c_3(t) \quad (2)$$

The time series of b_j and c_j describe the time dependence of all spatial derivatives. Some of our clusters consisted of only three buoys (K=3) or were reduced to three buoys by instrument failure. For these clusters the first-order polynomials in (2) provide an exact solution to the cluster velocity fields. Higher-order polynomials could be used for clusters with K>3 and, for perfect ice velocity data, would provide more accurate estimates of gradient parameters. We chose not to do this, however, so that the analysis methodology was consistent between different clusters, and our experience with higher-order fits is that they introduce unacceptable noise because of the buoy position errors. The latter difficulty is particularly relevant to Argos-tracked buoys: the more accurate and frequent position data from buoys navigated with the Global Positioning System (GPS) could be used to generate higher quality estimates of ice velocity gradients.

We create cluster-averaged time series of the differential kinematic parameters (DKPs) from time varying coefficients b_j and c_j: i=1…3 in (2), for example, the drift divergence,

$$\nabla \cdot \mathbf{D}(t) = \frac{\partial d_x}{\partial x} + \frac{\partial d_y}{\partial y} \approx b_1+c_2, \quad (3)$$

and drift vorticity,

$$\nabla_z \times \mathbf{D}(t) = \frac{\partial d_y}{\partial x} - \frac{\partial d_x}{\partial y} \approx c_1-b_2. \quad (4)$$

Approximate signal-to-error ratios for the quantities used to study ice dynamics on the basis of daily averaged data are shown in Table 1.

The assumption made in estimating ice divergence from (2) and (3) is that over the entire cluster and for each time step, the linear functions (2) used to fit $d_x(x,y)$ and $d_y(x,y)$ for the K buoys truly represent the ice motion field. In the real ocean, however, true measures of ice divergence require that the area occupied by an identifiable "patch" of sea ice can be accurately integrated or that ice velocity is defined and fully resolved around some closed perimeter. These methods are possible with synthetic aperture radar (SAR) when individual ice floes can be identified and tracked between pairs of SAR images [*Drinkwater*, 1998]. However, orbit characteristics of existing SAR data generally preclude resolution of feature motion at the timescales necessary for estimating tidal band divergence. For the present study therefore we use these buoy-derived tidal-band divergence estimates in a primarily qualitative way, in comparisons with divergence estimates from an ocean tidal model.

Time series of the linearized approximations to $\nabla\cdot\mathbf{D}$ and $\nabla_z\times\mathbf{D}$ were calculated for each cluster. Buoys from different deployment programs rarely overlapped in time, and so were never combined. Our previously defined frequency limits were used for exploring diurnal and semidiurnal DKP variability. In addition we defined a "weather band," which was obtained by low-pass filtering with a cutoff frequency of 1/36 cph. Wind forcing of ice motion occurs mainly at frequencies below this cutoff but also contributes some energy to the diurnal band and a smaller amount to the semidiurnal band.

The mean ($\langle$DKP$\rangle$) and standard deviation (σ(DKP)) of $\nabla\cdot\mathbf{D}$ and $\nabla_z\times\mathbf{D}$ for each frequency band were calculated for consecutive 30-day periods for each cluster, and these values were assigned to the mean positions of each buoy cluster and the central time for each analysis period (Table 2). The mean ice motion during the 30 day intervals was typically ~150 km and thus caused spatial averaging that is comparable to the spatial averaging inherent in the O(100) km separations of buoys within each cluster. There were occasions, however, where the mean drift exceeded 500 km during a 30 day period: this occurred for buoys in the northern Weddell Sea (see section 3).

Table 1. Typical Signal Magnitudes, Error Estimates, and Signal-to-Error Ratios for Daily Averaged Quantities Used to Study ice Dynamics

Quantity	Typical Signal Magnitude	Error Estimate	SER[a]
Drift vector components, cm s^{-1}	10	0.5	20
Ice drift divergence, $\times10^{-6}$ s^{-1}	0.3	0.1	3
Ice drift vorticity, $\times10^{-6}$ s^{-1}	0.6	0.1	6

[a]Signal-to-error ratio

3. Spatial Distribution of Mean Ice Speeds

Diurnal band ice speeds D_d >4 cm s^{-1} occur in many regions of the Weddell Sea (Plate 1a). The largest values, ~20 cm s^{-1}, are found over the southwestern continental shelf near 70.5°S, 57.5°W, where *Viehoff and Li* [1995] observed strong diurnal motions. (The drifter that they analyzed, 9357, is included in our analyses.) Values of $D_d \approx 10$ cm s^{-1} along the shelf break between 31° and 39°W are similar to those obtained from moored current meters (see Figure 1b for locations of ocean current data).

Values of D_{sd} (Plate 1b) over deep water are largest south of the Scotia Ridge and near 71°S, 28°W. Values of D_{sd} exceed 5 cm s^{-1} along almost all of the western and southern shelf break and the continental shelf north of the Ronne Ice Front. The largest mean current speeds (>7 cm s^{-1}) along the shelf break occur in the northern end of the Filchner Depression. These values are similar to those obtained from moored current meters.

Area-preserving spectra of ice motion for selected 30 day periods of individual buoys are shown in Figure 4. We show the raw spectral estimates for these records; hence the frequency bandwidth $\Delta\omega$ is 1/30 cpd ($\approx 2.4\times10^{-6}$ s^{-1}). The two dominant constituents in each of the tidal frequency bands (M_2 and S_2 in the semidiurnal band and O_1 and K_1 in the diurnal band) are therefore separated by one "nontidal" spectral estimate. Values of D_d and D_{sd} (here based on the analyzed 30 day record and not the 15 day records used for Plate 1) for each of these records are also shown in Figure 4. Remember that D_d and D_{sd} are determined from time series of ice drift that have been band passed with quite broad frequency limits (1/36 and 1/18 cph for the diurnal band and 1/18 and 1/6 cph for the semidiurnal band). These values therefore include not only the obvious tidal peaks but also broadband energy because of the ice response to wind and internal ice stresses.

Values of D_d and D_{sd} for the most westerly buoy in the ISW-1 cluster, Site Ed (Figure 4a), are both ~4 cm s^{-1}. Ice

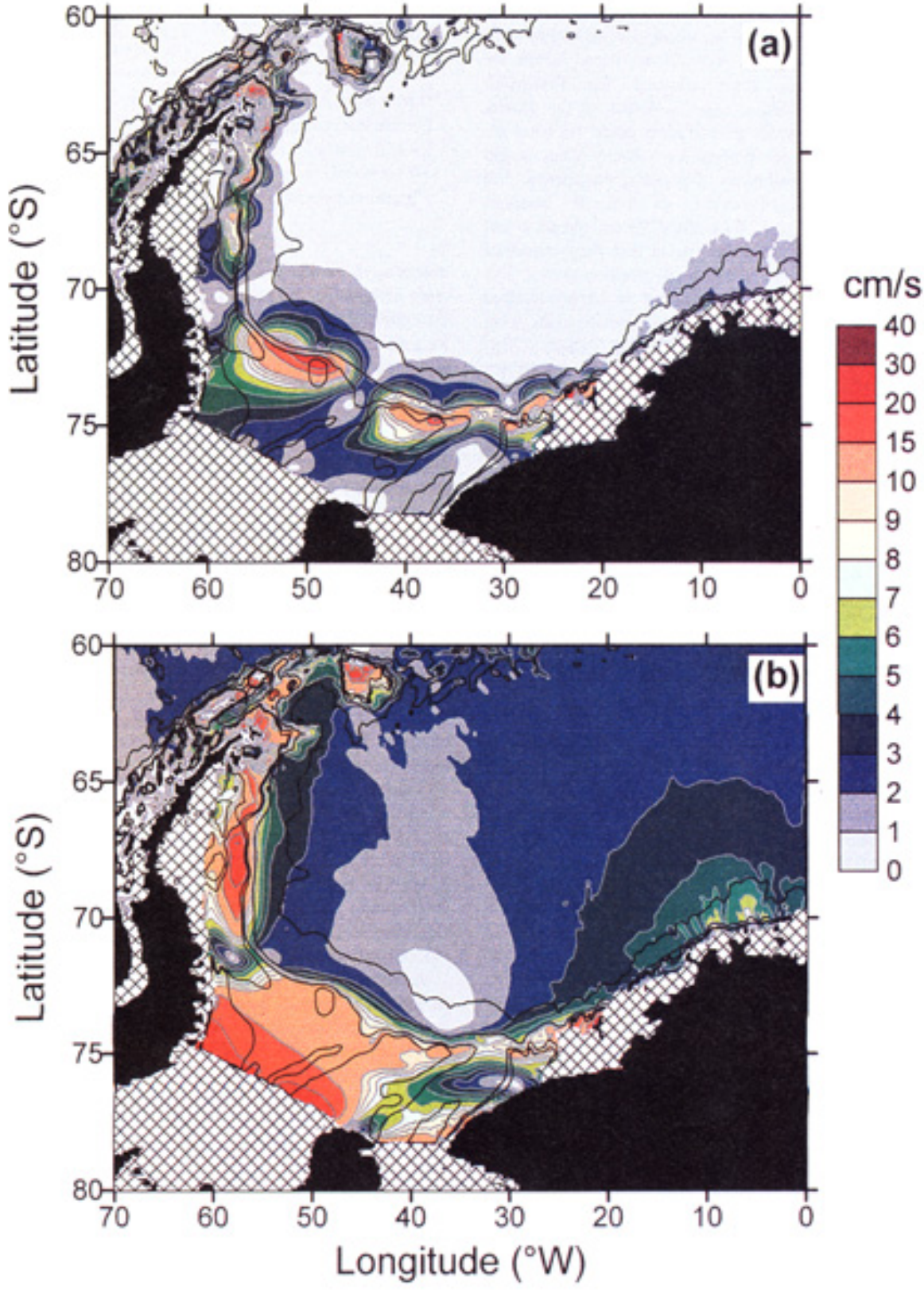

Plate 2. Modeled mean tidal current from CATS99.2 for (a) the diurnal band U_d, and (b) the semidiurnal band U_{sd}. The 400, 500, 1000, and 3000 m isobaths are shown as solid lines (see Figure 1). The color ranges are not evenly spaced.

Table 2. Standard Deviations for Divergence and Vorticity for Three Frequency Bands Described in Text: Weather Band, Diurnal, and Semidiurnal

Latitude	Longitude	Day of Year	Divergence			Vorticity		
			Weather	Diurnal	Semidiurnal	Weather	Diurnal	Semidiurnal
				Southwestern Inner Shelf				
-72.33	-59.18	75	0.7	1.1	0.9	1.1	1.6	1.0
-71.18	-59.10	106	0.6	1.7	1.1	0.9	1.2	1.4
-70.59	-59.27	136	1.1	0.9	0.7	0.7	1.2	0.7
				Southwestern Outer Shelf				
-71.47	-52.37	135	0.2	0.4	0.4	0.4	0.9	0.3
-71.38	-53.26	54	1.2	1.0	0.9	0.6	0.9	0.8
-70.42	-53.76	75	0.3	0.6	0.6	0.4	0.6	0.5
-72.86	-50.53	105	0.2	0.3	0.2	0.5	0.9	0.2
-71.71	-50.68	135	0.2	0.4	0.6	0.3	0.9	0.4
				Western Shelf				
-69.90	-59.45	167	0.5	0.9	0.6	0.8	0.9	0.5
-69.77	-53.50	166	0.2	0.2	0.1	0.5	0.5	0.2
-69.10	-59.49	197	0.3	0.4	0.6	0.4	0.5	0.5
-68.85	-59.44	228	0.4	0.4	0.5	0.4	0.4	0.5
-68.63	-59.19	246	0.5	0.4	0.4	0.4	0.3	0.4
-68.57	-53.42	106	0.3	0.4	0.6	0.4	0.4	0.5
-67.59	-54.73	196	0.0	0.0	0.1	0.3	0.3	0.1
-67.39	-52.90	196	0.4	0.6	1.1	0.4	0.3	0.2
-67.30	-53.29	136	0.2	0.4	0.6	0.3	0.5	0.5
-66.97	-54.89	227	0.1	0.2	0.2	0.4	0.4	0.2
-66.65	-53.15	227	0.1	0.2	0.2	0.5	0.4	0.3
-66.01	-53.64	258	0.5	0.2	0.3	0.5	0.4	0.3
-65.47	-51.44	258	0.4	0.2	0.3	0.7	0.4	0.4
				Ronne Depression				
-75.03	-49.03	50	0.6	0.2	0.3	0.6	0.4	0.3
-74.97	-58.01	28	1.1	0.7	0.7	0.6	0.5	0.6
-74.64	-50.79	53	0.6	0.2	0.3	0.4	0.3	0.4
-74.32	-50.37	74	0.3	0.1	0.2	0.8	0.2	0.3
-73.99	-59.08	45	1.9	0.8	1.0	2.5	1.3	0.9
-73.92	-51.90	74	0.3	0.1	0.2	1.0	0.2	0.2
				General Belgrano Bank				
-72.72	-44.85	105	0.4	0.5	0.6	0.7	1.1	0.6
-72.51	-52.20	105	0.2	0.3	0.2	0.5	0.7	0.2
				Filchner/Southern Slope				
-73.86	-37.74	74	1.5	2.4	0.9	1.7	2.1	1.2
				Southeastern Weddell Sea				
-73.74	-26.72	349	0.4	0.4	0.6	0.8	0.6	0.7
-72.83	-22.58	319	0.4	0.3	0.4	0.9	0.3	0.5
-71.28	-27.51	45	1.1	1.0	1.6	1.6	1.0	1.8
-70.83	-25.75	15	1.1	0.6	1.4	1.7	0.7	1.3
-69.94	-21.04	349	0.9	1.0	2.3	1.3	1.1	2.4
-69.83	-14.52	319	0.7	0.6	0.9	1.2	0.6	0.9
				Central Weddell Sea				
-71.81	-37.97	105	0.4	0.3	0.4	0.7	0.2	0.3
-71.23	-47.38	135	0.2	0.3	0.4	0.3	0.3	0.4
-70.36	-39.53	135	0.3	0.2	0.2	0.6	0.2	0.2
-69.45	-48.05	166	0.2	0.3	0.5	0.6	0.3	0.3
-68.62	-40.11	166	0.4	0.2	0.2	0.7	0.2	0.2
-67.77	-41.19	196	0.3	0.2	0.2	0.9	0.3	0.2
-67.76	-47.79	196	0.3	0.2	0.3	1.1	0.6	0.4
-66.27	-38.73	227	0.2	0.2	0.2	0.6	0.3	0.2
-65.69	-33.93	258	0.2	0.2	0.2	0.7	0.3	0.3
-65.57	-45.28	227	0.2	0.2	0.4	0.6	0.5	0.5
-65.18	-40.00	258	0.2	0.2	0.4	0.9	0.4	0.5
-65.03	-47.18	288	0.4	0.3	0.7	0.8	0.3	0.7
-64.28	-31.41	288	0.2	0.2	0.2	0.7	0.3	0.2
-63.53	-35.82	288	0.2	0.2	0.3	0.7	0.4	0.4
-63.14	-26.43	319	0.2	0.2	0.3	0.5	0.4	0.4
-62.20	-29.14	319	0.9	0.4	0.7	1.2	0.6	0.7

Standard deviations are given in units of 10^{-6} s^{-1}. Estimates are grouped by geographical area.

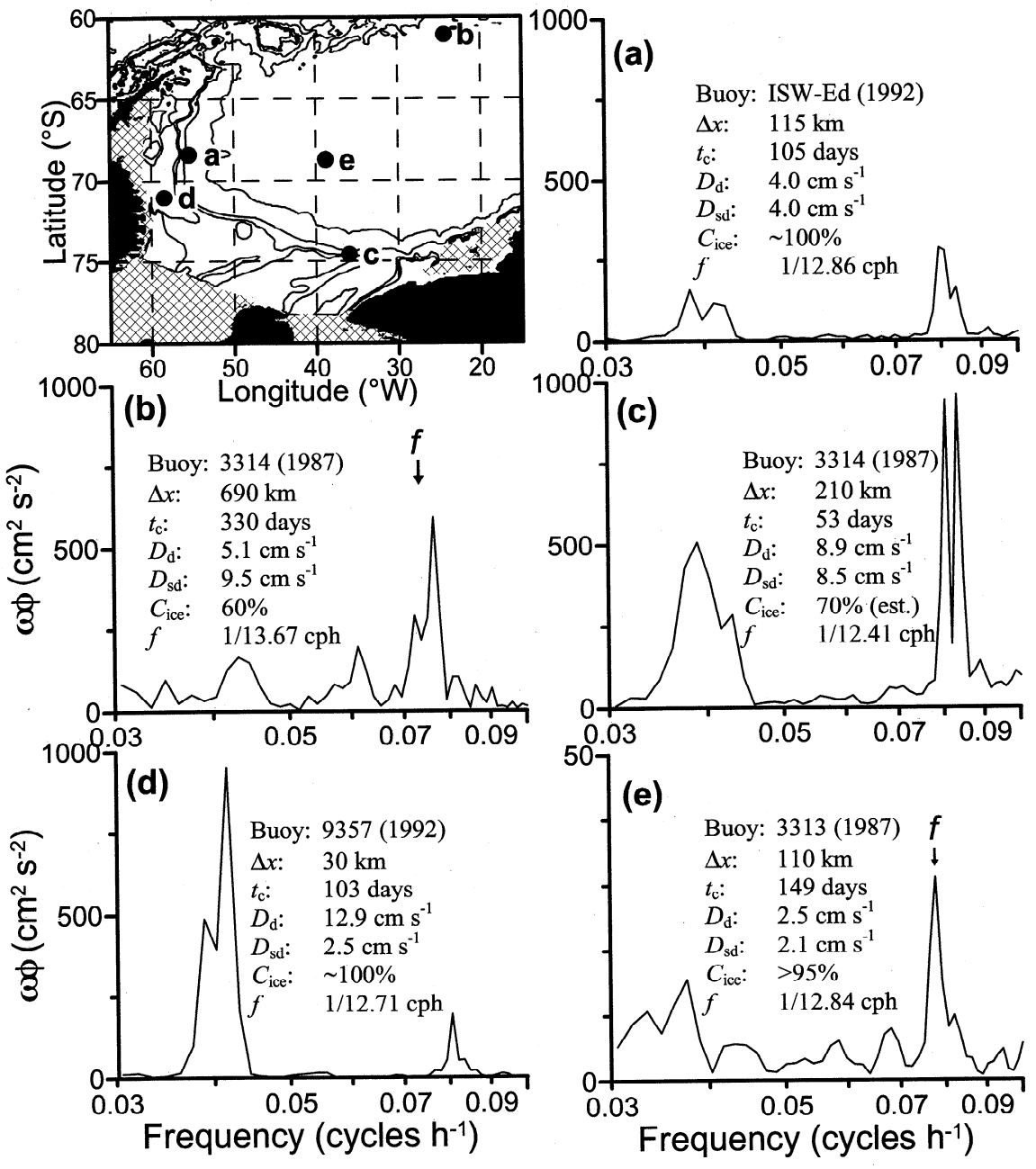

Figure 4. The map in the upper left shows the locations of the central points of each of five buoy drift tracks for which area-preserving spectra ($\omega\phi$, where $\phi=\phi_u+\phi_v$ is the sum of the power spectral densities for u and v) are shown in Figures 4a-4e. Spectra are based on 30 days of measured ice velocity. The total drift distance Δx, time in day of year at the center of the analysis period t_c, diurnal and semidiurnal mean ice drift speeds, D_d and D_{sd}, respectively, and estimated ice concentration C_{ice} based on SSM/I are shown for each record. The scale for $\omega\phi$ in Figure 4e is 20 times larger than for Figures 4a-4d. The frequencies for O_1, K_1, M_2, and S_2 are 0.0387, 0.0418, 0.0805, and 0.0833 cycles h^{-1}, respectively.

velocity was similar to upper ocean tidal currents measured at the same site [*Levine et al.*, 1997]. Mean ice concentration, based on SSM/I analyses and observations from helicopters, was close to 100% at this time.

In the northern Weddell Sea just south of the Scotia Ridge (Figure 4b), $D_d \approx 5$ cm s^{-1} and $D_{sd} \approx 10$ cm s^{-1}. There is significant energy in a broad frequency band between 0.07 and 0.08 cph (1/14.3 and 1/12.5 cph). The mean latitude for this record is ~61.1°S, giving $f \approx 1/13.7$ cph. We attribute most energy throughout this spectral peak to wind-forced near-inertial ice response. (A smaller spectral peak between 0.08 and 0.085 cph contains the M_2 and S_2 tidal energy.) While the spectral peak ($\approx$1/13.2 cph) is not precisely at f, the time series of u and v in the semidiurnal band (Figure 5) do appear to be dominated by near-inertial motion. As expected for near-inertial motion, u and v have similar magnitudes, with v lagging u by $\sim\pi/2$ (Figure 5). That is, the velocity vector traces out an almost circular ellipse rotating anticlockwise.

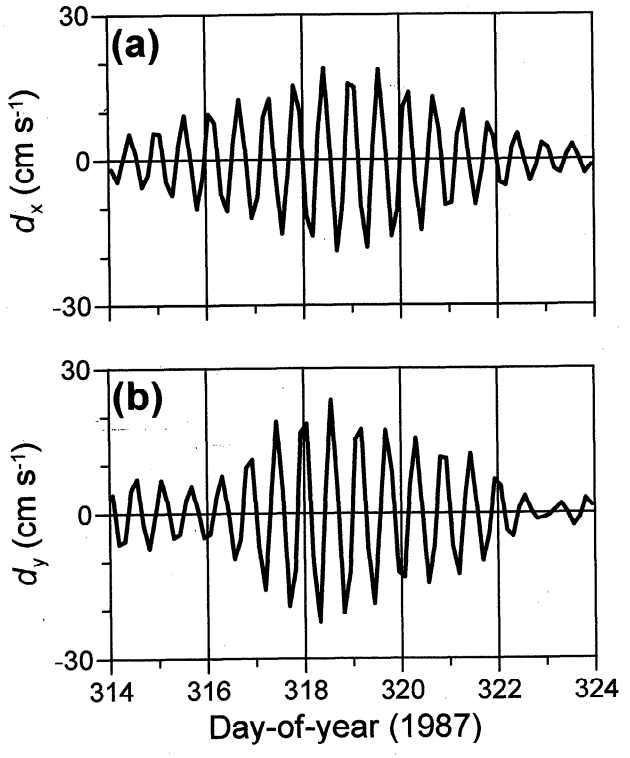

Figure 5. Time series of (a) d_x and (b) d_y for buoy 3314 in the northern Weddell Sea (see Figure 4b) after band passing between 1/15 and 1/11 cph (semidiurnal). Amplitudes of d_x and d_y are similar, and d_x leads d_y by ~$\pi/2$, consistent with anticlockwise, wind-forced near-inertial motion.

The largest observed inertial ice drift speed in the northern Weddell Sea data was ~25 cm s^{-1}, although more typical values are 5-10 cm s^{-1}. By looking at a longer time series we also find that the modulation of amplitude is less regular than we would expect from spring-neap cycling because of tides, with a timescale for amplitude variability of 5-10 days rather than the 14 days expected for a spring-neap cycle. This observation is consistent with the amplitude responding to the passage of storm fronts.

Along the southern shelf break near the northern Filchner Depression (Figure 4c), D_d and D_{sd} are each ~8-9 cm s^{-1}, which is comparable to local measured ocean tidal current speeds [*Middleton et al.*, 1987; *Foldvik et al.*, 1990]. The semidiurnal energy is seen as two narrow, separated peaks corresponding to the M_2 and S_2 tides (although f is not separable from M_2 at this latitude), while the diurnal band is broad, without clearly defined peaks for O_1 and K_1. The lack of separated peaks in the diurnal band can be explained by the 210 km net drift during the analysis period. For the semidiurnal constituents, amplitude and phase vary only slightly over this drift. However, most of the energy in the diurnal constituents is associated with short-wavelength (O(200) km), topographically trapped vorticity waves [*Middleton et al.*, 1987], so the phase and amplitude variations of each diurnal constituent are blurred in the analysis of ice drift even if the free drift approximation is valid. Ice concentration is estimated at ~70% at this time (February/March 1987). We will discuss the diurnal tide in more detail in section 4.2.

Over the southwestern shelf (Figure 4d), the spectrum of the same drifter record discussed by *Viehoff and Li* [1995] is dominated by the diurnal band. For this record the total drift during the 30 day period was only 45 km; hence the diurnal peak is narrower than for the location of Figure 4c. The value of D_d is ~13 cm s^{-1}. Ice concentration is >95% at this time (April 1992).

Over deep water in the central western Weddell Sea (Figure 4e), D_d and D_{sd} are small, each 2-3 cm s^{-1}. Note that the scale for the spectrum in Figure 4e is 20 times finer than for Figures 4a-d because there is so little ice drift kinetic energy at this site. The spectral peak in the semidiurnal band is at the inertial frequency of 1/12.84 cph, and very little tidal energy is present in either the diurnal or semidiurnal bands. Mean ice concentration is ~95% at this time (May/June 1987).

These spectra encompass the range of ice motion found in the Weddell Sea associated with both wind stress and tides and further modified by dependence on ice concentration. Clear tidal signals are found over the shelf and slope (Figures 4a, 4c, and 4d), where the tide may be predominantly diurnal or mixed diurnal-semidiurnal. For the two deep water sites (Figures 4b and 4e) there is no clear diurnal spectral peak, although values of D_d are 5 and 2 cm s^{-1}, respectively, in part because of the breadth of the frequency limits used to define this band. In the semidiurnal band an inertial response rather than tidal forcing dominates the ice motion. The near-inertial energy at the location of Figure 4b in the northern Weddell Sea is about 20 times greater than at the location of Figure 4e in the central western Weddell Sea, and we attribute this to a combination of much higher ice concentration and lower wind energy in the latter region.

The spectra in Figure 4 also demonstrate some of the difficulties in using ice motion for tidal analyses, even when C_{ice} is sufficiently low that we might expect the free drift approximation to apply. The most obvious difficulty is the contamination of the semidiurnal band by inertial motion. In addition, it is not always possible to resolve even the major tidal constituents because the buoy drift during the time interval needed to separate constituents can be large, thus moving the buoy through a region in which the tidal amplitudes and phases may change significantly. In the semidiurnal band this problem is significant only when the buoy drift is across isobaths so that tidal current amplitude changes rapidly. In the diurnal band, along-slope mean drift can blur the tidal spectra because much of the diurnal energy along the outer shelf and upper slope is associated with shelf-trapped topographic vorticity waves (TVWs). The TVWs have a short wavelength, O(200) km, so that phase varies rapidly along the slope, while amplitude varies rapidly across the slope. Thus, even a slow mean drift of 1-2 km d^{-1} (Δx=30-60 km over 1 month) might lead to significant broadening of the tidal spectral peaks.

Despite these difficulties, by limiting analyses to periods of buoy drift with small Δx and C_{ice}«100% it appears that useful information on ocean tidal currents may be obtained from measured ice motion. One difficulty with testing this hypothesis is the paucity of ocean tidal current data in much of the Weddell Sea. Our approach to mitigating this data limitation is to use an ocean tidal model to produce tidal speed maps that can be directly compared to the tidal band ice drift data from the buoys. This ocean model is described in section 4, including comparisons with the available ocean data.

4. Barotropic Ocean-Only Tidal Model

4.1. Model Overview

The barotropic, ocean-only, Circum-Antarctic Tidal Simulation, version 99.2 (CATS99.2) that we use here is an updated version of the Weddell/Scotia Seas model described by *Robertson et al.* [1998] (denoted RPE98.1). The CATS99.2 domain includes the entire ocean south of 50°S. The grid spacing is 1/4° x 1/12°, which gives ~10 km resolution near the Antarctic coast. For the ocean cavities under the Ross Ice Shelf (RIS) and Filchner and Ronne Ice Shelves (FRIS), we replace water depth with "water column thickness," i.e., the vertical distance between the base of the glacial ice and the seabed. The water column thickness values for the FRIS were obtained from *Johnson and Smith* [1997], and those for the RIS were kindly provided by D. Holland (personal communication, 1999). For all other ice shelves the water depth was taken unmodified from ETOPO-5 since very few glacier thickness data are available. The model incorporates depth data for the southwestern Weddell Sea that was acquired during the 1998 Ronne Polynya Experiment (ROPEX-98) [*Nicholls et al.*, 1998; *Padman et al.*, 1998, 1999].

Three diurnal (O_1, K_1, and Q_1) and five semidiurnal ($2N_2$, M_2, S_2, N_2, and K_2) tidal constituents are simulated. This set was chosen because these are the primary constituents in the finite-element simulation global tidal model (FES95.2) [*Le Provost et al.*, 1998] that we use for the open boundary condition along 50°S. The CATS99.2 model is run nonlinearly: the model solves the shallow water equations by forward time stepping with boundary conditions specified as the superposition of all eight constituents. Nonlinear responses, including additional tidal constituents and a mean tidal residual circulation, can develop through the advective terms, the quadratic bottom friction c_d, and the lateral viscosity A_H. The nonlinear terms are, however, typically small, and so, the model output is interpreted in terms of just the eight primary constituents and a mean flow term, Z_0. Analyses on the last 90 days of the model run were performed using methods following *Foreman* [1977, 1978], i.e., a least squares fit of phase-shifted sine waves with the frequencies of the eight primary constituents plus Z_0.

Sea ice is not included in CATS99.2. As will be shown in the section 4.2, the model comparison with current meter data is quite poor in the important diurnal band along the southern shelf break. We believe that it is premature to add ice dynamics before investigating ways to improve the ocean-only tidal solution for this region. In the semidiurnal band much of the energy in ice motion is due to near-inertial response to wind stress events. Despite these limitations in the ocean tidal model, comparing CATS99.2 with ice drift data will demonstrate the distribution of regions in which tidal currents influence ice motion and divergence in the Weddell Sea and will provide a basis for estimating tidal effects on ice divergence variance.

Before we compare the ocean tidal model and measured ice motion, however, we compare CATS99.2 with available tidal data in the Weddell Sea. This comparison will illuminate both the strengths and weaknesses of this model.

4.2. Model Validation

We consider here the performance of CATS99.2 only in the Weddell Sea. The most energetic semidiurnal tidal constituents are M_2 and S_2. In the diurnal band, O_1 and K_1 have similar structure and energy over most of the domain [*Robertson et al.*, 1998, Plate 1], except along the southern shelf break. We have compared the model with tidal elevation data in the Weddell Sea region. The results are not significantly different from those presented by *Robertson et al.* [1998, Figure 4]: most constituent amplitude and phase estimates agree with data within measurement uncertainty. Additional confidence in the model comes from satisfactory agreement with TOPEX/Poseidon altimetry data, which are available north of ~65°S. This result is not surprising since the FES95.2 model, from which the CATS99.2 northern boundary condition is obtained, has been tuned by assimilation of the TOPEX/Poseidon data [*Le Provost et al.*, 1998]. An independent validation of CATS99.2 comes from comparisons of model predictions with differential tidal displacements of the FRIS obtained from differential SAR interferometry (E. Rignot, et al., Observation of ocean tides below the Filchner-Ronne ice shelf, Antarctica, using synthetic aperture radar interferometry: Comparison with tide model predictions, submitted to *Journal of Geophysical Research*, 1999, hereinafter referred to as Rignot et al., submitted manuscript, 1999). On the basis of these different comparisons, CATS99.2 performs well at predicting tidal sea surface elevation in most of the Weddell Sea.

The tides' principal impact on ice motion is, however, through the stress applied by the ocean currents to the ice. Tidal currents are much more difficult to model accurately than sea surface elevation, especially in the diurnal band [see *Robertson et al.*, 1998, Figure 4]. In Table 3 and Figure 6 we compare the semimajor axes (U_{maj}) evaluated from CATS99.2 with values obtained from moorings over the southern continental shelf and slope (Figure 1b). The model consistently overestimates U_{maj} for M_2 and S_2 by $O(20)$%. We believe that this is due to the "critical latitude" effect [*Foldvik et al.*, 1990; *Nøst*, 1994; *Furevik and Foldvik*, 1996; *Robertson*, 1999]. A tidal constituent's critical latitude (λ_{crit}) is the latitude at which the tidal frequency equals $f(\lambda)$. These latitudes are ~74.47° and 85.76° for M_2 and S_2, respectively. Models and observations suggest that near λ_{crit} the constituent's momentum boundary layer can become extremely thick, up to several hundred meters. Most current data in our comparison come from within 100 m of the seabed (see Table 3); thus we expect these measurements to be within the benthic momentum boundary layer for the semidiurnal constituents, especially M_2. The current obtained from depth-integrated models will generally exceed the current measured in this boundary layer. With this in mind we regard Figure 6 as indicating satisfactory agreement in the semidiurnal band between the depth-integrated tidal model and the mooring measurements.

CATS99.2 represents O_1 and K_1 currents well along the Ronne Ice Front (points 9, 10, and 11) but significantly overestimates constituent amplitudes in the northern Filchner Depression and at most moorings on the southern slope. Comparisons between four model runs (RPE98.1, [*Padman et al.*, 1998a], the present study using CATS99.2, and the FES94.1 global model (P. Techine, personal communication, 1999) demonstrate that quite small changes to bathymetry near the shelf break can lead to large changes in predicted diurnal tidal currents along the southern shelf break. We conclude that even with the new depth data from ROPEX-98 [*Nicholls et al.*, 1998; *Padman et al.*, 1998, 1999], there is

Table 3. Semimajor U_{maj} and Semiminor Axes U_{min} and Ellipse Inclination I for the Four Principal Tidal Constituents (O_1, K_1, M_2, and S_2) From the CATS99.2 Tidal Model and Mooring Data Reported by *Foldvik et al.* [1990] and *Woodgate et al.* [1998]

Mooring ID	Mooring (z+)[a]	Location	Model Depth (m)	Variable	O_1		K_1		M_2		S_2	
					Mooring	Model	Mooring	Model	Mooring	Model	Mooring	Model
1	FMF-A[b]	southern	1915	U_{maj}	1.2	2.1	3.7	6.6	1.3	(2.6)	1.1	1.6
	(100 m)	slope		U_{min}	-0.6	-1.3	-1.8	-3.8	0.1	0.3	0.2	0.2
				I	16	46	25	59	64	66	43	63
2	FMF-B[b]	southern	720	U_{maj}	3.4	5.4	10.9	15.8	2.9	(6.1)	2.6	3.7
	(100 m)	slope		U_{min}	1.1	2.1	6.1	7.0	1.0	3.2	1.4	1.8
				I	66	51	66	61	72	66	76	66
3	FMF-C[b]	southern	475	U_{maj}	2.1	(5.8)	10.2	18.4	6.8	9.4	4.5	5.7
	(100 m)	slope		U_{min}	1.0	3.6	9.5	14.7	4.5	6.0	3.2	3.4
				I	84	35	49	53	74	68	72	69
4	FMF-D[b]	southern	465	U_{maj}	2.8	5.3	11.0	17.6	5.0	8.7	3.9	5.3
	(65 m)	slope		U_{min}	2.0	2.7	8.5	12.8	3.2	5.3	2.8	3.1
				I	55	41	19	57	46	68	54	69
5	FMF-E[b]	Filchner	475	U_{maj}	2.1	(8.1)	5.1	(14.2)	6.8	10.0	4.0	6.6
	(100 m)	Depression		U_{min}	1.2	7.4	4.2	11.9	4.2	6.0	2.3	3.7
				I	7	32	26	61	67	74	68	76
6	FMF-F[b]	southern	470	U_{maj}	8.4	6.5	15.4	25.5	2.2	(11.6)	1.7	(7.3)
	(25 m)	slope		U_{min}	5.2	1.1	11.3	12.7	0.7	6.2	0.5	3.7
				I	67	65	73	66	45	67	57	67
7	FR1[c]	Filchner	610	U_{maj}	1.2	(5.4)	2.5	(7.9)	5.7	9.0	3.6	6.1
	(353 m)	Depression		U_{min}	0.7	3.7	2.2	6.8	2.4	4.0	1.3	2.5
				I	13	-6	29	-2	63	71	67	73
8	FR2[c]	Filchner	509	U_{maj}	2.1	(5.7)	3.6	(8.0)	7.1	10.1	3.9	6.7
	(383 m)	Depression		U_{min}	1.2	4.3	3.1	7.1	4.0	5.2	1.8	3.2
				I	-8	-9	-2	0	62	71	61	73
9	FR3[c]	RIF[d]	284	U_{maj}	3.6	3.1	4.3	2.5	11.9	18.3	7.0	12.4
	(51 m)			U_{min}	0.5	0.8	0.5	1.0	0.9	-2.6	0.0	-2.1
				I	-52	-3	-22	46	30	20	28	19
10	FR5[c]	RIF[d]	598	U_{maj}	6.4	6.5	6.4	7.3	10.6	15.0	6.8	10.2
	(397 m)			U_{min}	-4.2	-4.6	-3.9	-4.3	-3.2	-3.5	-1.5	-2.3
				I	81	-89	77	90	58	57	59	57
11	FR6[c]	RIF[d]	665	U_{maj}	6.0	5.0	6.0	6.4	12.9	16.0	7.8	10.9
	(352 m)			U_{min}	-1.2	-1.7	-1.1	-1.9	-1.0	-2.3	-0.8	-1.5
				I	59	71	59	73	57	68	56	68
12	VL-95	Western	300	U_{maj}	9.3	18.5	10.9	18.9	3.4	6.3	1.3	(4.9)
	(ice drift)	Shelf		U_{min}	2.8	6.7	3.8	6.2	0.2	0.0	0.3	0.2
				I	-87	-85	-86	90	-1	5	-10	0

Where more than one current meter is on a mooring, the uppermost meter is used to minimize boundary layer effects. Ice drift values for the *Viehoff and Li* [1995] (VL-95) observations are included. Model values of U_{maj} in error by greater than a factor of 2 are shown in brackets. A negative sign for U_{min} implies that the current rotates clockwise; otherwise the current rotates counterclockwise.

[a]Here, z+ is the current meter height above the seabed.

[b]Mooring from *Foldvik et al.* [1990].

[c]Mooring from *Woodgate et al.* [1998].

[d]RIF is the Ronne Ice Front.

still insufficient bathymetric information in this region for accurate modeling of diurnal tidal currents. In the following paragraphs we discuss why diurnal constituents are more sensitive to bathymetry than are the semidiurnal constituents. In addition to errors caused by an inaccurate model depth grid, the amplitudes and phases of both O_1 and K_1 are known to vary, apparently seasonally [*Middleton et al.*, 1987, Figure 5], with the smallest amplitudes occurring in the austral winter (May-October). This latter observation is consistent with the propagation characteristics of the diurnal shelf waves being sensitive to seasonal changes in stratification [*Middleton et al.*, 1987] or to interactions between tides and wind-forced or thermohaline mean flows [*Foldvik et al.*, 1990]. Neither of these mechanisms is captured in depth-integrated, tide-only models such as CATS99.2.

For the reasons cited above it is not presently possible to predict time series of diurnal band tidal currents along the southern shelf break. It is possible however, to use CATS99.2 to estimate the statistics of ocean diurnal currents that are needed for comparison with the statistics of observed ice motion. From the data comparisons shown in Table 3 and Figure 6, the model overestimates U_{maj} for K_1 by factors of ~1.7 and 2 for the southern slope and northern Filchner Depression respectively. For the less energetic O_1 constituent the values are about ~2 and 3.5 for the same regions.

For estimates of divergence and other DKPs we may also need to understand the error in the instantaneous spatial gradients of tidal currents, represented by spatial gradients of constituent amplitudes and phases. Most tidal energy flux in the Weddell Sea is carried by the large-scale Kelvin waves

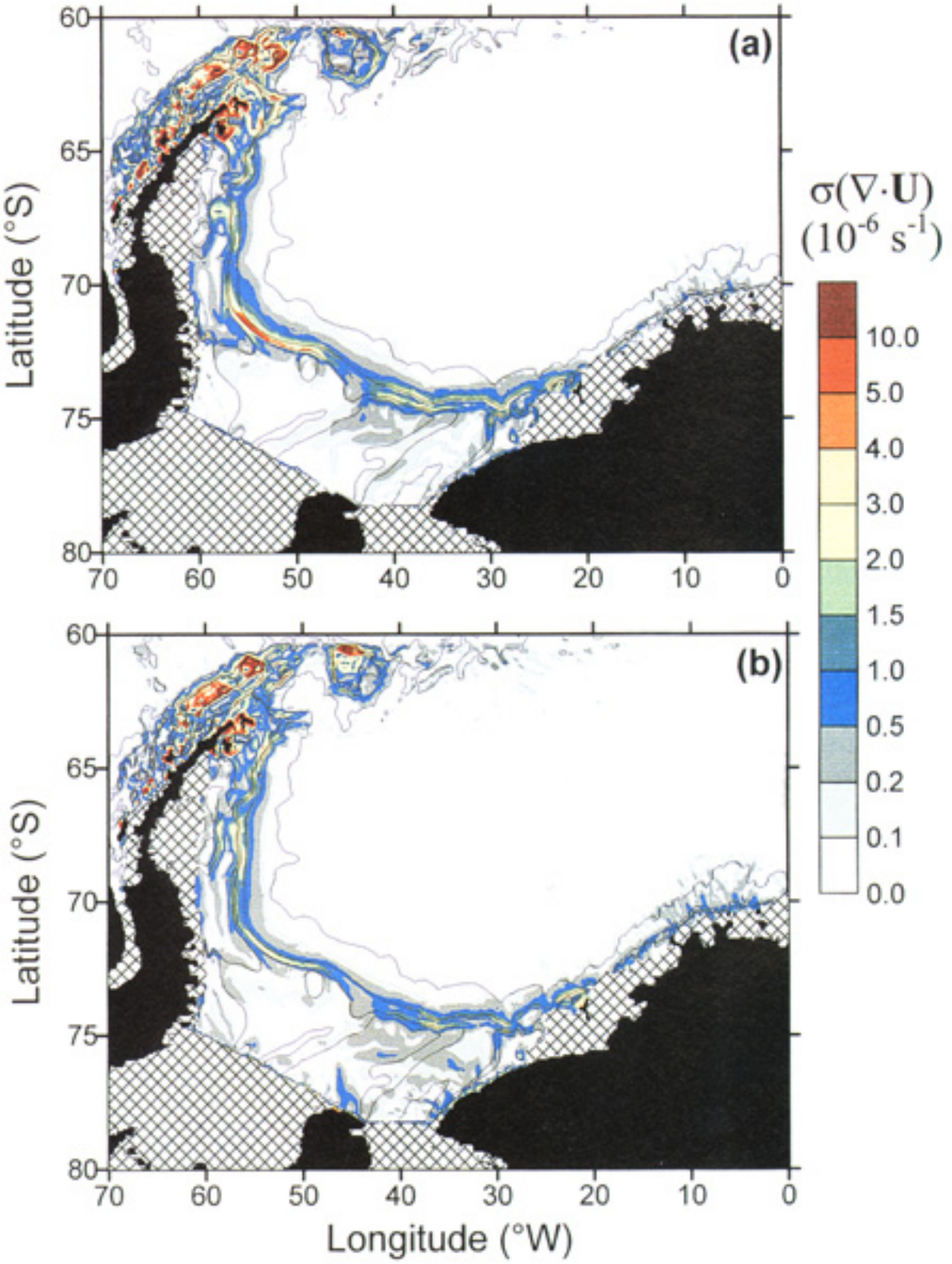

Plate 3. Standard deviation of horizontal divergence determined on ~100 km scale (in units of 10^{-6} s^{-1}) from the ocean-only depth-integrated CATS99.2 tidal model: (a) diurnal band (Q_1, O_1, and K_1) and (b) semidiurnal band ($2N_2$, N_2, M_2, S_2, and K_2). The 400, 500, 1000, and 3000 m isobaths are shown as solid lines (see Figure 1). The color ranges are not evenly spaced.

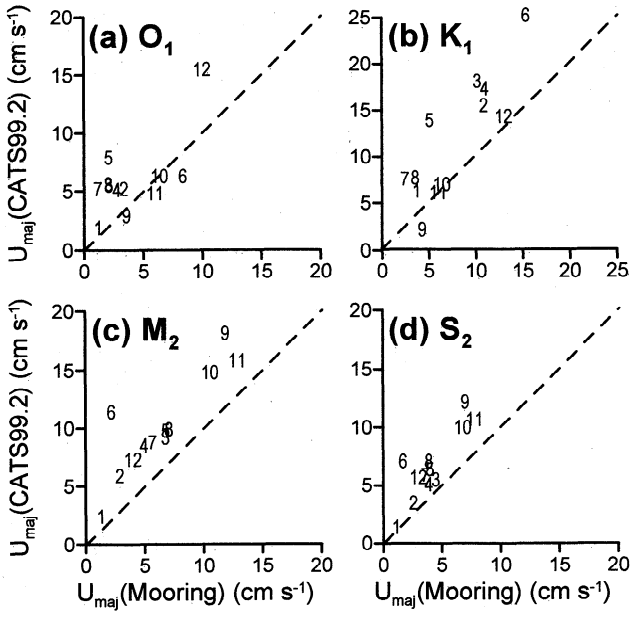

Figure 6. Comparison of semimajor axes U_{maj} (cm s^{-1}) between moored current meter measurements and the Circum-Antarctic Tidal Simulation, version 99.2 (CATS99.2) for (a) O_1, (b) K_1, (c) M_2, and (d) S_2 tidal constituents. Note the different scale for K_1. Dashed lines indicate model equivalence with data. Numbers on the plots refer to mooring identifiers in Table 3. Points 5, 7, and 8 are in the northern Filchner Depression. Points 9-11 are along the Ronne Ice Front, and point 12 is in the southwestern Weddell Sea. The remaining points come from moorings on the southern continental slope. Point 12 is actually a comparison of U_{maj} derived from ice velocity for buoy 9357 [see *Viehoff and Li*, 1995].

that propagate along the Antarctic coast. Their long length scales, $O(10^4)$ km wavelength and $O(10^3)$ km offshore decay scale, make these waves insensitive to small topographic errors, and they are therefore relatively easy to model. However, most diurnal tidal energy along the southern slope is associated with short-wavelength topographic vorticity waves (TVWs) [*Middleton et al.*, 1987]. The observed properties of these waves are qualitatively consistent with an analytical model of TVWs traveling along a long, straight slope between a wide continental shelf and a deep basin [*Saint-Guily*, 1976]. In this model, along-slope wavelength λ_y is sensitive to the shape of the continental slope, scaling directly with the characteristic slope width (denoted a), and also varying with the ratio of the depths of the shelf and the offshore deep basin. *Middleton et al.* [1987] measured values of λ_y for K_1 and O_1 TVWs of ~230 km and 120 km, respectively. These waves are also found in CATS99.2. In Figure 7 we show the phase of the K_1 and O_1 v velocity (roughly cross-slope) components along the southern shelf break from 56° to 20°W. Velocity phase is shown instead of sea surface elevation phase because kinetic energy in this region is mostly associated with the short-wavelength TVWs, whereas the potential energy is dominated by the tidal Kelvin waves. The model values of $\lambda_y(K_1)$ and $\lambda_y(O_1)$ near 39°W are ~340 km and 180 km, respectively, each being ~50% greater than the observed wavelengths. The value of a can change quite rapidly with along-slope distance: *Middleton et al.* [1987] noted that a varied from ~40 to 100 km in two cross-slope transects with an along-slope separation of <100 km. As expected from this observation, we also find a factor of 2 variability in modeled λ_y along the shelf break.

The observed short-wavelength TVWs have phase propagation toward the west but with group velocity (and energy) propagating eastward. Errors in modeling the energy of diurnal constituents at the moorings used in our comparisons (Figure 6) therefore probably arise from model shortcomings to the west of these moorings. This region, the western and southern continental slope, is the area of least depth data control in the model depth grid, and it will be difficult to improve models of tidal constituents without first improving the depth database. A second source of errors due to inadequate bathymetry data may be the artificial smoothness of the depth grid in the southwestern Weddell Sea. More realistic rougher bathymetry might scatter or otherwise dissipate more of the TVW energy than occurs in CATS99.2.

4.3. Spatial Distribution of Tidal Speed Estimates

Ice floes drift through regions of varying tidal amplitudes and phases during the time interval that is needed to resolve the major constituents. As shown in section 3 (see the ice velocity spectra in Figure 4), this net drift limits our ability to resolve individual constituents, especially in the diurnal band for the reasons discussed in section 4.2. Thus, in order to construct maps that can be directly compared with the ice

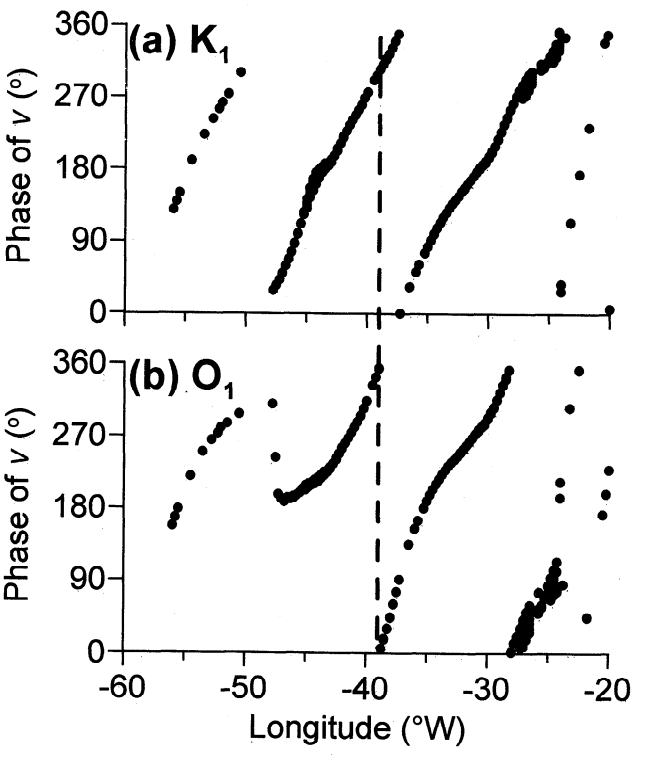

Figure 7. Phases of the v velocity component (roughly cross slope) for (a) K_1 and (b) O_1 as functions of longitude near the 750 m contour along the southern shelf break from CATS99.2. The approximate location of the current meters used in comparisons with the model is indicated with the vertical dashed line near 39°W.

motion speed maps (Plate 1), we define diurnal and semidiurnal band mean current speeds, U_d and U_{sd}, respectively. The values of U_d and U_{sd} are evaluated from a 90 day simulated time series of the tidal current speed at each model grid point using a superposition of all constituents in each frequency band (three diurnal and five semidiurnal).

Maps of U_d and U_{sd} are shown in Plate 2. The largest value of U_d is ~25 cm s^{-1} near the General Belgrano Bank (GBB), which is a submarine plateau centered near 73°S, 50°W. Much larger values were reported for this region by *Robertson et al.* [1998], but these were based on a model depth grid in which the GBB was a well-defined plateau that rose more than 200 m relative to the local mean shelf depth of 400-450 m. The new depth data from ROPEX-98 demonstrate that the GBB actually rises <50 m relative to the typical shelf depth and is really the eastern limit of a ridge extending westward to at least 58°W, just inshore of the shelf break. Values of U_d exceed 10 cm s^{-1} along most of the shelf break of the southern and western Weddell Sea (Plate 2a). Recall, however, that the model values of U_d along the southern slope near the northern Filchner Depression are typically 1.5-2 times as large as current meter moorings indicate (Figure 6). Over most of the deep basin, U_d<1 cm s^{-1}.

The largest values of U_{sd} (Plate 2b) occur over the outer western continental shelf and along the Ronne Ice Front. Values of U_{sd} over most of the deep basin are <3 cm s^{-1}, and typical values over the shelf are ~10 cm s^{-1}. As discussed in section 4.2, the modeled semidiurnal currents agree well with ocean current measurements throughout the southern Weddell Sea after considering the boundary layer response to proximity to critical latitude and the locations of the current meters above the seabed.

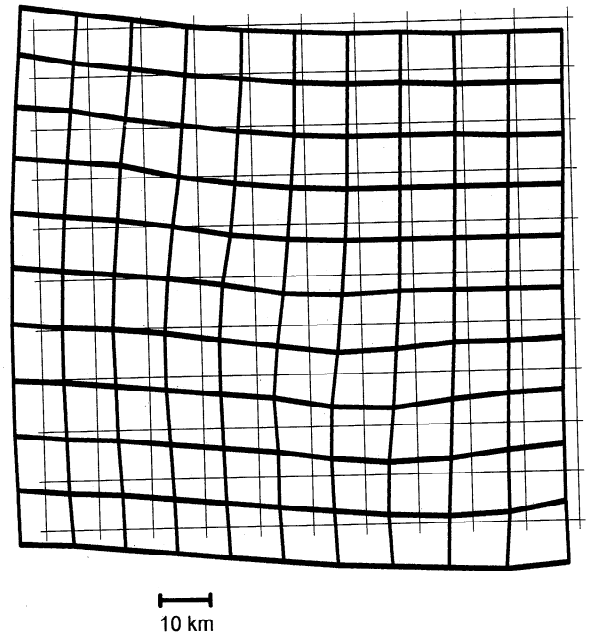

Figure 8. Distortion of an initially regular 11x11-element array centered near 71.3°S, 55.2°W (southwestern shelf break) for 12 hours of tidal advection. During these 12 hours, particles at each node of the initial grid (thin lines) have been tracked with bicubic interpolation within the time-dependent tide model grid to the final positions (thick lines). The period shown represents diurnal spring tide, that is, O_1 and K_1 currents are approximately in phase. The total area of the grid increases by 8.9%: areas of individual cells increase by between 1.3 and 31.6%.

4.4. Spatial Distribution of Modeled Ocean Tidal Divergence

We wish to use our ocean-only depth-integrated tidal model to estimate tidal band ice divergence statistics. To this end we first equate the surface current with the modeled depth-averaged ocean velocity vector $\mathbf{U}(x,y,t)$. The limited ocean data suggest that this is a reasonable first approximation. The horizontal divergence at a location with water depth $H(x,y)$ is then balanced by the time rate of change in surface elevation η at that point,

$$\nabla \cdot (H\mathbf{U}) + \frac{\partial \eta}{\partial t} = 0 . \qquad (5)$$

When H is constant the divergence is simply $-H^{1}\partial\eta/\partial t$, which we shall call the "Eulerian" divergence, denoted $(\nabla\cdot\mathbf{U})_E$. However, a water column that is advected over a sloping bottom experiences a "Lagrangian" divergence that can be much larger than $(\nabla\cdot\mathbf{U})_E$. We see this by rewriting the conservation of volume for a water column in Lagrangian terms as

$$H\left(\frac{\partial u}{\partial x} + \frac{\partial v}{\partial y}\right) + \left(u\frac{\partial H}{\partial x} + v\frac{\partial H}{\partial y}\right) + \frac{\partial \eta}{\partial t} = 0 , \qquad (6)$$

i.e.,

$$H\nabla \cdot \mathbf{U} + \frac{\mathrm{D}H}{\mathrm{D}t} + \frac{\partial \eta}{\partial t} = 0 . \qquad (7)$$

In (7), $\mathrm{D}H/\mathrm{D}t$ is the Lagrangian (along-path) time derivative of water depth and is typically much greater than $\partial\eta/\partial t$. Volume conservation requires that the Lagrangian rate of change of fractional area $(\nabla\cdot\mathbf{U})_L$ be inversely proportional to the rate of change of fractional water depth ($H^{1}\mathrm{D}H/\mathrm{D}t$) due to advection.

We can visualize this distortion by modeling the trajectories of an initially regular grid of Lagrangian particles. Particle displacements are shown in Figure 8 for a small region centered on 71.3°S, 55.2°W, these coordinates being chosen within a region of large divergence variance along the southern shelf break (see Plate 3). Trajectories were obtained by time-integrating particle velocities for an 11x11-element array in our tidal model. We chose a 12 hour integration time to represent a half-tidal cycle in this diurnally dominated region. The simulation was run at diurnal band spring tide (O_1 and K_1 roughly in phase). Mean displacements for individual particles vary significantly over the grid, both in speed and direction. The result is a distortion of what we associate here with a field of noninteracting surface particles (e.g., ice assuming free drift). The ratio of final to initial cell area for this array ranges from 1.01 to 1.32, and the summed array area increases by 8.9%. In regions of shallow and steep topography a small column of water is easily advected into a region where the area averaged water depth is significantly different from the mean water depth at the start of the trajectory. As the length scale of the advected region becomes large relative to the average advection distance, however, the fractional change in area averaged water depth is reduced,

implying a smaller horizontal divergence. As was discussed in section 2.3, the geometry of the buoy clusters and the choice of 30 day analysis intervals results in a length scale of $O(100)$ km for DKP calculations, and a similar length scale should be used in the model when comparing DKPs from the two methods.

Maps of the standard deviation of horizontal divergence of ocean tidal currents for the diurnal and semidiurnal tidal frequency bands (denoted $\sigma(\nabla\cdot\mathbf{U}_d)$ and $\sigma(\nabla\cdot\mathbf{U}_{sd})$, respectively) are calculated from CATS99.2 (Plate 3). We obtain these values by first synthesizing hourly time series of the tidal current velocity field over 90 days at all locations in the model domain. We then calculate $\nabla\cdot\mathbf{U}(x,y,t)$ for 50%-overlapping 11x11-element arrays, i.e., a characteristic length scale of $O(100)$ km. Finally, the standard deviation as a function of position only, $\sigma(\nabla\cdot\mathbf{U})$, is determined from $\nabla\cdot\mathbf{U}(x,y,t)$ in the usual way. We include the Lagrangian divergence terms (7) due to tidal advection across local gradients of water depth. The largest values of $\sigma(\nabla\cdot\mathbf{U}_d)$, excluding a region near the tip of the Antarctic Peninsula, occur in a narrow band along the southern and western shelf break. A typical value of $\sigma(\nabla\cdot\mathbf{U}_d)$ in energetic regions is 1-2x10^{-6} s^{-1}, with a maximum value of ~6x10^{-6} s^{-1}. For comparison, a typical value of total ice drift divergence standard deviation (including weather band variability) over the Weddell Sea is ~0.3x10^{-6} s^{-1} [*Kottmeier et al.*, 1997]. Values of $\sigma(\nabla\cdot\mathbf{U}_d)$ in the deep basin and much of the broad southern shelf are negligible (<0.1x10^{-6} s^{-1}). There is a very narrow band of high $\sigma(\nabla\cdot\mathbf{U}_d)$ (>0.5x10^{-6} s^{-1}) along the Ronne Ice Front that is not easily seen in Plate 3.

Since the Lagrangian term in (7) dominates the model estimates of $\sigma(\nabla\cdot\mathbf{U}_d)$ over the continental slope, $\sigma(\nabla\cdot\mathbf{U}_d)$ depends almost entirely on the magnitude of cross-slope tidal current and not on the spatial scales of current variability. Thus the critical feature of the error in diurnal band modeled currents is the overestimation of $|\mathbf{U}_d|$ rather than the error in the wavelengths and cross-slope spatial scales of the diurnal TVWs (see section 4.2). As we showed in section 4.2 (see also Figure 6), the semimajor axes for the dominant diurnal constituent K_1 are overestimated by the model by a factor of ~1.7 on the southern slope, and 2 in the northern Filchner Depression. We can therefore estimate the true value of $\sigma(\nabla\cdot\mathbf{U}_d)$ as being ~50% of the modeled value in this region. (Where the diurnal currents are adequately modeled by CATS99.2, for example, along the Ronne Ice Front (points 9, 10, and 11 in Figure 6), no reduction should be made in the modeled values of $\sigma(\nabla\cdot\mathbf{U}_d)$). Even when the appropriate scaling is applied to the map of $\sigma(\nabla\cdot\mathbf{U}_d)$, the values along the shelf break greatly exceed typical values in the central Weddell Sea.

In the semidiurnal band (Plate 3b), the largest values of $\sigma(\nabla\cdot\mathbf{U}_{sd})$ are found along the southern and western outer continental shelves. The largest values of $\sigma(\nabla\cdot\mathbf{U}_{sd})$ here are typically >0.5x10^{-6} s^{-1}. Values of $\sigma(\nabla\cdot\mathbf{U}_{sd})$ also exceed 0.5x10^{-6} s^{-1} in a very narrow band along the Ronne and Filchner Ice Fronts, although this is not easily seen in Plate 3b. Remember that the comparison between CATS99.2 and ocean tidal data (Figure 6) suggests that the model values of semidiurnal currents are quite accurate. We therefore believe that the model values of $\sigma(\nabla\cdot\mathbf{U}_{sd})$ are reasonable estimates of the divergence standard deviation of ice velocity due to tidal stresses when the free drift approximation is valid.

5. Discussion

5.1. Ice Drift Velocities

We postulated that ice response to ocean tidal currents can often be adequately represented by free drift models (see section 2.1): this is a necessary condition for inferring ice divergence from the modeled ocean current divergence (Plate 3). Is free drift ever a valid assumption in areas of interest to us? We compare tidal band ice drift with analyses of current meters and CATS99.2 predictions for three moorings near the northern Filchner Depression (Table 4). Ice concentration based on SSM/I data was ~70% at the time the drifters were in this region. As we have noted previously, diurnal currents are not well modeled by CATS99.2 in the Filchner Depression; however, the measured values of U_d from the moorings match D_d quite well. In the semidiurnal band the mooring and model values of U_{sd} both agree well with D_{sd}. In Figure 9, we compare time series of d_x and d_y in the semidiurnal band for drifter 3314, with u and v ($\mathbf{U}_{model}$) in the semidiurnal band predicted with CATS99.2. Values of $\mathbf{U}_{model}(x,y,t)$ were obtained for the time and location of each buoy estimate of position and velocity, thus $\mathbf{U}_{model}$ includes both temporal variability and spatial variation of constituent amplitudes and phases along the buoy's drift track. The agreement between the two time series demonstrates that the free drift approximation is reasonable here. Similar time series comparing diurnal band observed ice velocity and modeled ocean currents (not shown) demonstrate that as expected from Table 4, diurnal currents are not well modeled. However, the comparison of diurnal band energy in the ice motion and moored current meter data (Table 4) and the validation of the free drift assumption in the semidiurnal band (Figure 9), lead us to expect that diurnal band ice motion will also be strongly correlated with true ocean diurnal tidal currents. These observations will be relevant to our discussion of tidal band ice divergence in section 5.2.

Table 4: Tidal currents in the Southern Shelf/Slope Region and Filchner Depression at the Sites of Three Current Meter Moorings Reported by *Foldvik et al.* [1990] and *Middleton et al.* [1987]

Mooring (Location)	Tidal Band	Current, cm s^{-1}		
		U_{meas}	Model	Ice Motion
FMF-A (slope)	Diurnal	4	5	5
	Semidiurnal	2	2	(5)
FMF-D (shelf)	Diurnal	12	15	9
	Semidiurnal	8	6	8
FMF-E (Filchner Depression)	Diurnal	6	(14)	7
	Semidiurnal	9	8	8

Instrument depths and water depth at the moorings are given in Table 2. Measured currents U_{meas} are evaluated from the RMS amplitudes presented by *Middleton et al.* [1987]. U_{meas}(diurnal)= $(\sigma^2(O_1)+\sigma^2(K_1))^{1/2}$, and U_{meas}(semidiurnal)=$(\sigma^2(M_2)+\sigma^2(S_2))^{1/2}$. Model mean current speeds (U_d and U_{sd}) and mean ice drift speeds (D_d and D_{sd}) are given for the same locations. Quantities that are poor fits to the mooring data (factor of 2 or greater mismatch) are indicated by brackets.

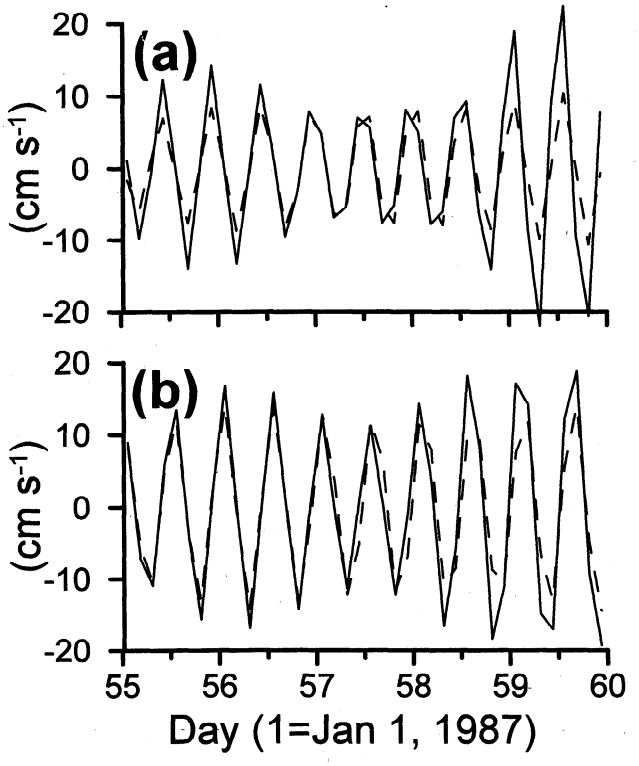

Figure 9. Time series of semidiurnal band ice drift velocity components (solid lines) from buoy 3314 near the northern Filchner Depression in February 1987 compared with modeled semidiurnal current components (dashed lines) from the CATS99.2 tidal model: (a) easterly components d_x and u_{model} and (b) northerly components d_y and v_{model}.

The other data set for which similar comparisons can be attempted is ISW-1 in the western Weddell Sea [*Muench and Gordon*, 1995; *Geiger et al.*, 1998a, b]. Here we consider data from Site Ed for the period centered near day 105 in 1992 (see spectrum in Figure 4a). The only direct current data for comparison is from 50 m below the ice [*Levine et al.*, 1997]. Measurements at other stations in the ISW-1 cluster, however, indicate that the tidal current at 50 m is similar to deeper currents. The modeled current ($\mathbf{U}_{\mathrm{model}}$) from CATS99.2 is quite similar to the measured current in this portion of the drift of Site Ed for both diurnal and semidiurnal bands. The ice motion is also closely coupled to $\mathbf{U}_{\mathrm{model}}$ (Figure 10); thus we feel confident that CATS99.2 can be used to estimate ice motion in this region even though C_{ice} from SSM/I at this time was close to 100%.

In the deep ocean, modeled tidal currents are small, typically <2 cm s^{-1}. This model-based observation is consistent with measured tidal current speed values obtained from moorings deployed across the central Weddell Sea [see *Fahrbach et al.*, 1994]. Tidal band ice speeds frequently exceed the equivalent ocean tidal current values. Values of D_d (Plate 1a) are similar to the tidal values in the central Weddell Sea, but increase to ~5 cm s^{-1} north of ~67°S. We suggest two reasons for this variability in wind-forced tidal-band ice motion. First, lower values are found in the region of net ice convergence in the western central Weddell Sea (excluding areas of tidal influence on the shelf and slope), suggesting that mean ice concentration is a factor. Spatial variability in the wind-forced component of D_d may also be related to the factor of 2 variation in total wind variance [*Kottmeier et al.*, 1997], which increases toward the north. Similar variation is found in D_{sd} (Plate 1b), although in this case the values in the northern Weddell Sea are much larger than D_d. Since wind energy in the semidiurnal band is lower than in the diurnal band, we postulate that most of the wind-forced semidiurnal band ice motion is due to the inertial near-resonant response of the ice to passing weather fronts. This response is only seen when C_{ice} is relatively low, as in the northern Weddell Sea and in a region centered near 70°S, 27°W, where the drifters were present during the time of year when C_{ice} was low.

As we showed in section 4.2, for the sites over the southern shelf and continental slope where current measurements have been obtained, the CATS99.2 tidal model performs well at predicting semidiurnal tidal currents. The model also performs well in the diurnal band along the Ronne Ice Front and in comparisons with data from ISW-1 in the western Weddell Sea. Additional support for the model comes from favorable comparisons between model predictions and ice shelf vertical displacement measured by differential SAR interferometry (Rignot et al., submitted manuscript, 1999) and by three-dimensional GPS measurements on the Ekström Ice Shelf near 8°W [*Riedel et al.*, 1999]. The major weakness in CATS99.2 is that it overestimates diurnal tidal kinetic energy along the southern shelf break. Diurnal tides in this region exist as TVWs (see section 4.2), which have along-slope wavelengths of $O(200)$ km and dispersion properties that are sensitive to cross-slope bathymetry. We believe that model

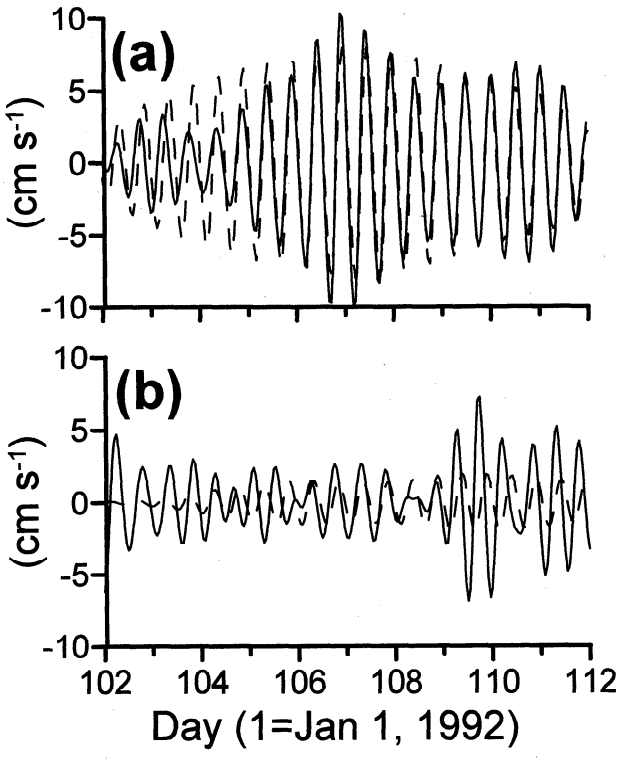

Figure 10. Time series of semidiurnal band ice drift velocity components (solid lines) from Ice Station Weddell 1, Site Ed, near the western continental shelf break in 1992 compared with modeled semidiurnal current components (dashed lines) from the CATS99.2 tidal model: (a) easterly components d_x and u_{model} and (b) northerly components d_y and v_{model}.

errors stem from two primary sources, inaccuracy of the depth grid and insufficient wave dissipation and dispersion because of the smoothness of the model depth grid. We are studying several methods to improve diurnal predictions including the introduction of realistic bathymetric roughness and formal inverse modeling with data assimilation of tidal currents in the southern Weddell Sea. In the meantime, however, we obtain estimates of the influence of the diurnal tide in this region by reducing the predicted currents by ~50% (see Table 3 and Figure 6) along the southern shelf break and in the northern Filchner Depression.

This study suggests to us that ice motion obtained from ice-mounted satellite-tracked drifters can be used to help determine the underlying ocean tidal current field in the Weddell Sea. Since C_{ice} is readily observable by satellite, the data quality from a specific buoy can be assessed by comparison with the local values of C_{ice}. On the basis of our analyses a rule of thumb is that ice motion should be closely coupled to ocean tidal currents for C_{ice} < ~80%. If the ice motion were used in a formal data assimilation scheme to improve the predictive skill of a regional tidal model, the acceptable error covariance could be made an increasing function of C_{ice}. Ice motion estimates would then provide a more rigid constraint on the inverse model when C_{ice} was lower. The Weddell Sea is an ideal environment for using such nontraditional techniques for improving tidal models. Depth-integrated tidal models generally work well because the ocean stratification is too weak to support a strong baroclinic tide, and standard ocean data are difficult to obtain.

Additional techniques for improving tide models include attempts to use ERS-1 and ERS-2 satellite altimetry over sea ice to measure directly the tidal variability (S. Laxon, personal communication, 1998) in a manner similar to the use of TOPEX/Poseidon altimetry over open water [*Egbert et al.*, 1994; *Egbert*, 1997]. Iceberg groundings [*Viehoff and Li*, 1995] and satellite or airborne gravity surveys used to interpolate between ship tracks [*LaBrecque and Ghidella*, 1997; *Smith and Sandwell*, 1997] are also valuable tools for improving the depth grids used by dynamical tidal models.

5.2. Ice Divergence Due to Tides

The reasonable agreement between semidiurnal ice drift and ocean tidal currents predicted using CATS99.2 suggests that at least in regions where tidal energy is high and C_{ice} is significantly below 100%, the free drift approximation (1) is valid. We therefore believe that the contribution of semidiurnal tides to high-frequency divergence standard deviation under these conditions can be estimated from CATS99.2. In the diurnal band, CATS99.2 overestimates tidal currents along the southern shelf break by about a factor of 2. Although the model also overestimates the spatial scales of the diurnal TVWs that dominate the energy in this region, this error does not significantly effect the divergence estimates, which are dominated by the Lagrangian term (area changes because of conservation of volume as the water column is advected across isobaths). That is, $\sigma(\nabla\cdot\mathbf{U}_d)$ scales directly with the cross slope velocity at the shelf break and so, for a rough approximation to the true value of $\sigma(\nabla\cdot\mathbf{U}_d)$, we can reduce the CATS99.2 values of $\sigma(\nabla\cdot\mathbf{U}_d)$ by ~50%. After this scaling is taken into account the standard deviation of total (i.e., diurnal plus semidiurnal) tide-forced divergence at the shelf break has a typical value of 1×10^{-6} s^{-1}, with maximum values of ~2.5×10^{-6} s^{-1}. The largest values are found in narrow strips along the continental shelf break and the fronts of the FRIS. Over deep water, $\sigma(\nabla\cdot\mathbf{U}_d)$ and $\sigma(\nabla\cdot\mathbf{U}_{sd})$ are both negligible (<0.1×10^{-6} s^{-1}).

Tidal band ice divergence was also estimated from least squares fitting of linear functions for drift velocity components of small clusters of ice-mounted satellite-tracked buoys, as described in section 2.3 (Table 2). This fitting method is best suited to studies of processes such as wind-forced mean divergence, where the characteristic spatial scale of the divergence is larger than the buoy cluster scale. When tides are the dominant source of ocean variability, the characteristic scales of ice motion are related to length scales of topographic variability, and thus the potential exists for unresolved structure in ice velocities to compensate for the apparent divergence in velocity fields that have been linearized according to (2). Despite this caveat we find that the method generates distributions of $\sigma(\nabla\cdot\mathbf{D}_d)$ and $\sigma(\nabla\cdot\mathbf{D}_{sd})$ that are qualitatively consistent with estimates from CATS99.2. The largest area-averaged values are found over the southwestern shelf, Filchner Depression and southern slope (only one point), and the southeastern Weddell Sea. The largest values tend to occur during the austral oceanographic summer (December-March), and with the limitations of the existing database, it is difficult to separate spatial variability from a seasonal dependence on ice concentration. Nevertheless, buoy-derived divergence values in regions where tides are energetic and C_{ice} is well below 100% frequently exceed 0.5×10^{-6} s^{-1} and are sometimes >1×10^{-6} s^{-1}. These values are similar to the maximum values of $\sigma(\nabla\cdot\mathbf{U})$ obtained with the ocean tidal model. The agreement between divergence estimates is not surprising since for C_{ice} < ~80%, we found that ice motion was consistent with the free drift approximation. Over deep water, typical values of $\sigma(\nabla\cdot\mathbf{D}_d)$ and $\sigma(\nabla\cdot\mathbf{D}_{sd})$ from the buoy clusters are $0.2\text{-}0.3\times10^{-6}$ s^{-1} and so are significantly higher than predicted by the tidal model. Most of the divergence variance over deep water is therefore due to spatial variability in high-frequency wind stress and the inertial near-resonant response of the ice. Further contributions to measured divergence are provided by buoy position errors and noise introduced by the linearized fit to drift velocities within each cluster using (2).

The maximum increase in fractional lead area $\Delta A.A^{-1}$ due to periodic tidal divergence can be estimated from

$$C_{L,\max}=\Delta A.\langle A\rangle^{-1}=\pi\sigma(\nabla\cdot\mathbf{D})\omega^{-1}, \qquad (8)$$

where ω is the tidal frequency (in units of s^{-1}). Thus the value of $\sigma(\nabla\cdot\mathbf{D})=0.3\times10^{-6}$ s^{-1} for the deep water, where the motion is predominantly near-inertial (semidiurnal), corresponds to $C_{L,\max}\approx0.7\%$. For a diurnal-dominated divergence standard deviation of $\sigma(\nabla\cdot\mathbf{D})=2\times10^{-6}$ s^{-1} near the shelf break, however, $C_{L,\max}\approx9\%$. The mean lead area during the tidal cycle is roughly $C_{L,\max}/2$; thus the latter case corresponds to a mean lead area of ~4-5%.

What effect will this lead fraction have on area-averaged ocean-to-atmosphere heat flux? For this order-of-magnitude calculation we use a typical winter net ocean-to-atmosphere heat flux of 200 W m^{-2} for open water [*Launiainen and Vihma*, 1994] and 5 W m^{-2} through the second-year ice of the western Weddell Sea [*Robertson et al.*, 1995; *Lytle and Ackley*, 1996]. For C_{ice}=100%, the area mean flux $\langle F\rangle$ is simply 5 W m^{-2}; however, with 5% leads, $\langle F\rangle\approx15$ W m^{-2}. This scenario corresponds to free drift ice response to tides in a region of solid ice cover. At such high values of C_{ice} however,

we do not expect free drift to be valid and so, the actual mean lead fraction will be less than predicted by the tide model, and the lead contribution to $\langle F \rangle$ will also be reduced. Now, assume that the ice concentration without the influence of tides is 90% so that we might expect free drift to be a reasonable assumption. Then, $\langle F \rangle$ is ~25 W m^{-2} without the addition of tidal lead fraction and 35 W m^{-2} with tides added. Under these conditions the fractional increase in $\langle F \rangle$ due to tides is much less than for $C_{ice} \approx 100\%$; however, the real tidal contribution to $\langle F \rangle$ is probably greater because the tides really do modify the lead fraction. For comparison the average heat loss from Weddell Deep Water as it circulates clockwise from the prime meridian to the tip of the Antarctic Peninsula is ~20 W m^{-2} [*Fahrbach et al.*, 1994]. In summary, for tide-forced ice divergence in strongly tidal regions ($\sigma(\nabla \cdot \mathbf{D}) = 1\text{-}2 \times 10^{-6}$ s^{-1}), an additional 5-10 W m^{-2} may be lost from the ocean to the atmosphere in winter. Ice productivity and the associated salinity flux to the upper ocean are also enhanced (O. Eisen, personal communication, 1999).

The modeled mean tide-induced lead fraction (~2-5%) along the southern slope is consistent with the trough of relatively low mean ice concentration (C_{90}) that roughly follows the shelf break (Figure 3). Other features that are seen in Figure 3, such as the low probability of high ice concentration along the Ronne Ice Front and north of Berkner Island, are not necessarily related to tides. Katabatic winds flowing off the Ronne Ice Shelf maintain the Ronne Polynya, although possibly aided by tidal shear and strain [*Foldvik and Gammelsrød*, 1988]. Grounded icebergs on the Berkner Bank just northeast of the tip of Berkner Island interfere with the generally westward sea ice drift in this region [*Nøst and Østerhus*, 1998], causing a buildup of ice to the southeast of the icebergs and reduced sea ice concentration to the west. It is possible that the trough along the shelf break is also related to nontidal processes. However, the coincidence of $\sigma(\nabla \cdot \mathbf{D})$, $\sigma(\nabla \cdot \mathbf{U})$, and this low-concentration trough is supporting evidence for an influence of tides on ice dynamics for at least part of the year.

On the basis of our analyses of ice motion spectra as summarized in Figure 4, we conclude that the near-inertial response of the ice to wind stress is much more energetic for $C_{ice} \ll 100\%$ than for $C_{ice} \approx 100\%$. The spectrum in the northern Weddell Sea, where $C_{ice} \approx 60\%$ (Figure 4b), is dominated by energetic near-inertial motion, while the inertial response in the central western Weddell Sea, where $C_{ice} > 95\%$, is very weak (Figure 4e). It is tempting to assume that ice response to tides will follow the same pattern, i.e., substantially weaker when ice concentration is high. This expectation is consistent with a study of ice drift and ocean currents in the tide-dominated eastern Arctic [*Padman et al.*, 1992]. Nevertheless, the two spectra from regions of high ice concentration ($C_{ice} > 95\%$) in the western Weddell Sea (Figures 4a and 4d) indicate significant tidal influence. The model ocean tidal current component time series and the ice drift time series at ISW-1 Site Ed (Figures 4a and 10) are also well correlated. We suspect that high ice concentration is less effective at damping tidal motion in the ice than the near-inertial response to wind stress because the length scales of tidal variability are typically much larger than those of inertial motion. As the length scales of tidal current variability decrease, however, for example close to the shelf break where cross-slope amplitude variability is large and the diurnal TVW along-slope wavelengths can be short, we expect the free drift approximation to be less valid for large values of C_{ice}. Since this is the region where tidal frequency ocean divergence is largest, we assume for the present study that the true values of $\sigma(\nabla \cdot \mathbf{D}_d)$ and $\sigma(\nabla \cdot \mathbf{D}_{sd})$ are reduced relative to the tidal modeled tide free drift values ($\sigma(\nabla \cdot \mathbf{U}_d)$ and $\sigma(\nabla \cdot \mathbf{U}_{sd})$).

Values of $\sigma(\nabla \cdot \mathbf{U})$ are large in narrow bands along the shelf break and the Ronne Ice Front (Plate 3); however, over most of the Weddell Sea they are $<0.1 \times 10^{-6}$ s^{-1}. The averages of tidal model values $\sigma(\nabla \cdot \mathbf{U}_d)$ and $\sigma(\nabla \cdot \mathbf{U}_{sd})$ over the Weddell Sea south of 65°S and west of 20°W (a total area of ~2×10^6 km^2) are ~0.12×10^{-6} s^{-1} in each band. For calculating the value of $\sigma(\nabla \cdot \mathbf{U}_d)$ we assume that the true value of $|\mathbf{U}_d|$ along the southern shelf break is 50% of the modeled value, on the basis of the comparisons with moored current meter data (Figure 6). The buoy-derived average values of $\sigma(\nabla \cdot \mathbf{D}_d)$ and $\sigma(\nabla \cdot \mathbf{D}_{sd})$ for the central Weddell Sea are 0.23 and 0.35×10^{-6} s^{-1} (see Table 2). That is, the contribution of tides to divergence variance, when averaged over the entire western Weddell Sea, is significantly less than the measured average value. When the damping effect of ice internal stresses are taken into account, we expect the area-averaged tidal contribution to divergence variance to be even smaller than is suggested by these estimates based on free drift.

The shelf break and Ronne Ice Front are, however, regions that are crucial to setting the thermohaline characteristics of the entire Weddell Sea, thus the role of tide-forced divergence may be more significant than is implied by this simple area-averaging. High-salinity shelf water (HSSW) at the Ronne Ice Front is the source water for ice shelf water (ISW) that is formed when HSSW melts the glacial ice base under the FRIS. The salinity of HSSW and its production rate will determine the properties of ISW and the flux of ISW flowing north to the shelf break via the Filchner Depression. Open water along the Ronne Ice Front in winter increases the salinity of HSSW.

At the shelf/slope front, which is typically near the 600 m isobath, cold and saline shelf water types (HSSW and ISW) mix with the warm, salty Weddell Deep Water and Modified Warm Deep Water. The resulting water types are dense and sink down the continental slope, ultimately contributing to the formation of AABW and Weddell Sea Bottom Water. The increase in the density of surface water in winter because of the increased local ice production and consequent salt flux associated with the tide-induced mean lead fraction will contribute to the efficiency of dense water production and also modify the dynamics of the shelf/slope front.

Quantitative estimates of the effect of high-frequency lead fraction on average air-sea heat fluxes, ice formation, and salt flux to the upper ocean in the western Weddell Sea were evaluated by O. Eisen and C. Kottmeier, who used a kinematic-thermodynamic sea ice model and the measured time series of ice divergence for a single buoy cluster. Their study demonstrates that high-frequency ice divergence contributes ~10% of the total net heat flux and ice formation and almost 40% of the total salt flux into the upper ocean in this region.

We conclude that there is sufficient evidence of tidal influence on ice motion, divergence variance, and the associated winter air/sea heat and salt fluxes over the shelf and upper slope to justify additional improvements in tidal models for the Weddell Sea. Planned improvements include development of inverse models that are capable of

assimilating nontraditional tidal information such as shelf ice displacements (detected by differential SAR interferometry) and sea ice motion from ice-mounted satellite-tracked buoys. The focus of these efforts is the improvement in model skill for diurnal shelf waves along the continental shelf break. With improved ocean tidal modeling capability it would also be appropriate to develop a coupled ocean-ice model, initially with a dynamics-only ice component but ultimately including full thermodynamics. This effort would serve two purposes. It would allow us to quantify more rigorously the role of tidal divergence on ocean/atmosphere heat and salt exchanges and ice production, extending the application of the methods of O. Eisen and C. Kottmeier to the entire Weddell Sea and not simply to the areas in which buoy cluster motion data are available. It would also allow us to separate tidal from wind-forced near-inertial ice motion, which will be valuable in interpreting ice velocity maps obtained from ice feature tracking in SAR image pairs where tides and inertial motion usually appear as strongly aliased signals.

Acknowledgments. We thank Lutz Sellmann for processing the buoy data. Conversations with Mark Drinkwater inspired LP's interest in tidal forcing of ice motion. The National Snow and Ice Data Center provided satellite ice concentration data for Figure 3. Robin Robertson developed the initial version of the Weddell Sea tides model, and Lana Erofeeva ran the CATS99.2 model. Susan Howard provided additional modeling support, and Philippe Techine provided model output and bathymetry information for the FES94.1 and FES95.2 global tidal models. Eberhard Fahrbach provided most of the current meter data to which we refer in this paper. We thank Captain Tim Barton, the officers, and crew of *HMS Endurance* for helping us obtain the ROPEX-98 bathymetric data used to update our ocean tides model depth grid. LP was funded by grants OPP-9317319, OPP-9317321, and OPP-9615525 from the National Science Foundation. The drifter programs were funded by the German Ministry of Research and Technology under grants 5138391KF 40020 and 07KFT61 to the Universities of Hannover and Bremen and by the Alfred-Wegener Institute for Polar and Marine Research. We thank Igor Polyakov and Cathy Geiger for providing numerous excellent suggestions that were used to improve this manuscript.

References

Augstein, E., *The Winter Expedition of RV "Polarstern" to the Antarctic*, Alfred Wegener Inst. for Polar and Mar. Res., Bremerhaven, Germany, 1986.

Broecker, W. S., et al., How much deep water is formed in the Southern Ocean?, *J. Geophys. Res.*, *103*, 15,833-15,843, 1998.

De Veaux, R. D., A. L. Gordon, J. C. Comiso, and N. E. Bacherer, Modeling of topographic effects on Antarctic sea-ice using multivariate adaptive regression splines, *J. Geophys. Res.*, *98*, 20,307-20,319, 1993.

Drinkwater, M., Satellite microwave radar observations of Antarctic sea ice, in *Analysis of SAR Data of the Polar Oceans*, edited by C. Tsatsoulis and R. Kwok, pp 145-187, Springer-Verlag, New York, 1998.

Egbert, G. D., Tidal data inversion: Interpolation and inference, *Prog. Oceanogr.*, *40*, 53-80, 1997.

Egbert, G. D., A. F. Bennett, and M. G. G. Foreman, TOPEX/Poseidon tides estimated using a global inverse model, *J. Geophys. Res.*, *99*, 24,821-24,852, 1994.

Fahrbach, E., G. Rohardt, M. Schröder, and V. Strass, Transport and structure of the Weddell Gyre, *Ann. Geophys.*, *12*, 840-855, 1994.

Fahrbach, E., M. Schröder, and A. Klepikov, Circulation and water masses in the Weddell Sea, in *Physics of Ice-Covered Seas*, edited by M. Leppäranta, pp. 569-604, Helsinki Univ. Press, Helsinki, 1998.

Foldvik, A., and T. Gammelsrød, Notes on Southern Ocean hydrography, sea-ice and bottom water formation, *Palaeogeogr. Palaeoclimatol. Palaeoecol.*, *67*, 3-17, 1988.

Foldvik, A., J. H. Middleton, and T. D. Foster, The tides of the southern Weddell Sea, *Deep Sea Res., Part A*, *37*, 1345-1362, 1990.

Foreman, M. G. G., Manual for tidal heights analysis and prediction, *Pac. Mar. Sci. Rep. 77-10*, 97 pp., Inst. of Ocean Sci., Patricia Bay, Sidney, B.C., Canada, 1977.

Foreman, M. G. G., Manual for tidal currents analysis and prediction, *Pac. Mar. Sci. Rep. 78-6*, 70 pp., Inst. of Ocean Sci., Patricia Bay, Sidney, B.C., Canada, 1978.

Furevik, T., and A. Foldvik, Stability at M_2 critical latitude in the Barents Sea, *J. Geophys. Res.*, *101*, 8823-8837, 1996.

Geiger, C. A., S. F. Ackley, and W. D. Hibler III, Sea ice drift and deformation processes in the western Weddell Sea, in *Antarctic Sea Ice: Physical Processes, Interactions, and Variability, Antarct. Res. Ser.*, vol. 74, edited by M. O. Jeffries, pp. 141-160, AGU, Washington, D. C., 1998a.

Geiger, C. A., W. D. Hibler III, and S. F. Ackley, Large-scale sea ice drift and deformation: Comparison between models and observations in the western Weddell Sea during 1992, *J. Geophys. Res.*, *103*, 21,893-21,914, 1998b.

Gordon, A. L., Western Weddell Sea thermohaline stratification, in *Ocean, Ice, and Atmosphere: Interactions at the Antarctic Continental Margin, Antarct. Res. Ser.*, vol. 75, edited by S. S. Jacobs and R. F. Weiss, pp. 215-240, AGU, Washington, D. C., 1998.

Gordon, A.L., and Ice Station Weddell Group of Principal Investigators and Chief Scientists, Weddell Sea exploration from Ice Station, *Eos Trans. AGU*, *74*, 124-126, 1993.

Johnson, M. R., and A. M. Smith, Seabed topography under the southern and western Ronne Ice Shelf, derived from seismic surveys, *Antarct. Sci.*, *9*, 201-208, 1997.

Jokat, W., and H. Oerter (Eds.), The expedition ANTARKTIS-XII/3 with RV "*Polarstern*", *Rep. on Polar Res.*, *219*, Alfred Wegener Inst. for Polar and Mar. Res., Bremerhaven, Germany, 1997.

Kottmeier, C., and L. Sellmann, Atmospheric and oceanic forcing of Weddell Sea ice motion, *J. Geophys. Res.*, *101*, 20,809-20,824, 1996.

Kottmeier, C., J. Olf, W. Frieden, and R. Roth, Wind forcing and ice motion in the Weddell Sea region, *J. Geophys. Res.*, *97*, 20,373-20,383, 1992.

Kottmeier, C., et al., Wind, temperature and ice motion statistics in the Weddell Sea, *WMO Tech. Doc. 797*, 48 pp., 1997.

Kowalik, Z., and A. Y. Proshutinsky, The Arctic Ocean Tides, in *The Polar Oceans and Their Role in Shaping the Global Environment, Geophys. Monogr.*, vol. 85, edited by O. M. Johannessen, R. D. Muench, and J. E. Overland, pp. 137-158, AGU, Washington, D. C., 1994.

LaBrecque, J. L., and M. E. Ghidella, Bathymetry, depth to magnetic basement, and sediment thickness estimates from aerogeophysical data over the western Weddell Basin, *J. Geophys. Res.*, *102*, 7929-7945, 1997.

Launiainen, J., and T. Vihma, On the surface heat fluxes of the Weddell Sea, in *The Polar Oceans and Their Role in Shaping the Global Environment, Geophys. Monogr.*, vol. 85, edited by O. M. Johannessen, R. D. Muench, and J. E. Overland, pp. 399-419, AGU, Washington, D. C., 1994.

Le Provost, C., F. Lyard, J. M. Molines, M. L. Genco, and F. Rabilloud, A hydrodynamic ocean tide model improved by assimilating a satellite altimeter-derived data set, *J. Geophys. Res.*, *103*, 5513-5529, 1998.

Levine, M. D., L. Padman, J. H. Morison, and R. D. Muench, Internal waves and tides in the western Weddell Sea: Observations from Ice Station Weddell, *J. Geophys. Res.*, *102*, 1073-1089, 1997.

Lytle, V. I., and S. F. Ackley, Heat flux through sea ice in the western Weddell Sea: Convective and conductive transfer processes, *J. Geophys. Res.*, *101*, 8853-8868, 1996.

Maykut, G. A., The surface heat and mass balance, in *Geophysics of Sea Ice*, edited by N. Untersteiner, pp. 395-463, Plenum, New York, 1986.

Middleton, J. H., T. D. Foster, and A. Foldvik, Diurnal shelf waves in the southern Weddell Sea, *J. Phys. Oceanogr.*, *17*, 784-791, 1987.

Muench, R. D., and A. L. Gordon, Circulation and transport of water along the western Weddell Sea Margin, *J. Geophys. Res.*, *100*, 18,503-18,515, 1995.

Nansen, F., *Farthest North*, vol. 1, George Newnes, London, 1898.

Nicholls, K., L. Padman, and A. Jenkins, First physical oceanography results from the ROPEX98 cruise in the southern Weddell Sea, Filchner-Ronne Ice Shelf Program, Rep. 12, pp. 51-58, Alfred Wegener Inst., Bremerhaven, Germany, 1998.

Orsi, A. H., W. D. Nowlin Jr., and T. Whitworth III, On the circulation and stratification of the Weddell Gyre, *Deep Sea Res., Part I, 40*, 169-203, 1993.

Nøst, E., Calculating tidal current profiles from vertically integrated models near the critical latitude in the Barents Sea, *J. Geophys. Res., 99*, 7885-7901, 1994.

Nøst, O. A., and S. Østerhus, Impact of grounded icebergs on the hydrographic conditions near the Filchner Ice Shelf, in *Ocean, Ice, and Atmosphere: Interactions at the Antarctic Continental Margin, Antarct. Res. Ser.*, vol. *75*, edited by S. S. Jacobs and R. F. Weiss, pp. 267-284, AGU, Washington, D. C., 1998.

Padman, L., A. J. Plueddemann, R. D. Muench, and R. Pinkel, Diurnal tides near the Yermak Plateau, *J. Geophys. Res., 97*, 12,639-12,652, 1992.

Padman, L., K. W. Nicholls, and R. A. Robertson, Modelling tides in the southern Weddell Sea: Updated model with new bathymetry from ROPEX, Filchner-Ronne Ice Shelf Program, Rep. *12*, pp. 65-73, Alfred Wegener Inst., Bremerhaven, Germany, 1998.

Padman, L., K. W. Nicholls, and R. A. Woodgate, The 1998 Ronne Polynya Experiment (ROPEX), Antarct. J. U. S., in press, 1999.

Riedel, B., U. Nixdorf, M. Heinert, A. Eckstaller, and C. Mayer, The response of the Ekström Ice Shelf in the grounding zone to tidal forcing, *Ann. Glaciol.*, in press, 1999.

Rignot, E., Radar interferometry detection of hinge-line migration on Rutford Ice Stream and Carlson Inlet, Antarctica, *Ann. Glaciol., 27*, 25-32, 1998.

Robertson, R. A., Mixing and heat transport mechanisms in the upper ocean in the Weddell Sea, Ph.D. thesis, College of Oceanic and Atmos. Sci., Oregon State Univ., Corvallis, 1999.

Robertson, R. A., L. Padman, and G. D. Egbert, Tides in the Weddell Sea, in *Ocean, Ice, and Atmosphere: Interactions at the Antarctic Continental Margin, Antarct. Res. Ser.*, vol. 75, edited by S. S. Jacobs and R. F. Weiss, pp. 341-369, AGU, Washington, D. C., 1998.

Robertson, R. A., L. Padman, and M. D. Levine, Fine structure, microstructure, and vertical mixing processes in the upper ocean in the western Weddell Sea, *J. Geophys. Res., 100*, 18,517-18,535, 1995.

Rowe, M. A., C. B. Sear, S. J. Morrison, P. Wadhams, D. W. S. Limbert, and D. R. Crane, Periodic motions in the Weddell Sea pack ice, *Ann. Glaciol., 12*, 145-151, 1989.

Saint-Guily, B., Sur la propagation des ondes de seconde classe le long d'un talus continental, *C. R. Acad. Sci. Ser. B, 282*, 141-144, 1976.

Smith, W., and D. Sandwell, Global sea floor topography from satellite altimetry and ship depth soundings, *Science, 277*, 1956-1962, 1997.

Spindler, M., G. Dieckmann, and D. Thomas, The Expedition ANT-X/3 of RV "Polarstern" 1992, *Rep. Polar Res., 121*, Alfred Wegener Inst., Bremerhaven, Germany, 1993.

Thorndike, A. S., and R. Colony, Sea ice motion in response to geostrophic winds, *J. Geophys. Res., 87*, 5845-5852, 1982.

Viehoff, T., and A. Li, Iceberg observations and estimation of submarine ridges in the western Weddell Sea, *Int. J. Remote Sens., 16*, 3391-3408, 1995.

Woodgate, R. A., M. Schröder, and S. Østerhus, Moorings from the Filchner Trough and the Ronne Ice Shelf Front: Preliminary results, Filchner-Ronne Ice Shelf Program, Rep. *12*, pp. 85-90, Alfred Wegener Inst., Bremerhaven, Germany, 1998.

C. Kottmeier, Institut für Meteorologie und Klimaforschung, Universität Forschungszentrum Karlsruhe, Kaiserstr. 12, 76128 Karlsruhe, Germany. (ckottmei@imkhp6.physik.uni-karlsruhe.de)

L. Padman, Earth and Space Research, 1910 Fairview Avenue E., Suite 102, Seattle, WA 98102-3620. (padman@esr.org)

(Received April 30, 1997; revised August 30, 1999; accepted September 29, 1999.)